

# Unique contributions of parvalbumin and cholinergic interneurons in organizing striatal networks during movement

Howard J. Gritton<sup>1,6</sup>, William M. Howe<sup>1,2,6</sup>, Michael F. Romano<sup>1,6</sup>, Alexandra G. DiFeliceantonio<sup>1,2,3</sup>, Mark A. Kramer<sup>4</sup>, Venkatesh Saligrama<sup>5</sup>, Mark E. Bucklin<sup>1</sup>, Dana Zemel<sup>1</sup> and Xue Han<sup>1\*</sup>

**Striatal parvalbumin (PV) and cholinergic interneurons (CHIs) are poised to play major roles in behavior by coordinating the networks of medium spiny cells that relay motor output. However, the small numbers and scattered distribution of these cells have hindered direct assessment of their contribution to activity in networks of medium spiny neurons (MSNs) during behavior. Here, we build on recent improvements in single-cell calcium imaging combined with optogenetics to test the capacity of PVs and CHIs to affect MSN activity and behavior in mice engaged in voluntary locomotion. We find that PVs and CHIs have unique effects on MSN activity and dissociable roles in supporting movement. PV cells facilitate movement by refining the activation of MSN networks responsible for movement execution. CHIs, in contrast, synchronize activity within MSN networks to signal the end of a movement bout. These results provide new insights into the striatal network activity that supports movement.**

Movement disorders, including Parkinson's disease and Tourette syndrome, are hypothesized to result from disruptions of basal ganglia circuitry<sup>1–4</sup>. Within the basal ganglia, the dorsal striatum serves as a point of integration between cortical and subcortical regions that transforms information provided by these inputs to an output signal that guides behavior<sup>5,6</sup>. Medium spiny projection neurons are the major target of these inputs as well as the primary source of projections from the striatum. These cells comprise roughly 95% of all striatal neurons<sup>7,8</sup>, and are traditionally classified based on the target of their output in the globus pallidus and the presence of dopamine D1 (direct pathway) or D2 (indirect pathway) receptors<sup>9</sup>. Imbalance between these pathways is thought to contribute to the expression of motor pathologies<sup>2,10,11</sup>. Despite having disparate projection pathways and being differentially regulated by dopamine, recent calcium ( $\text{Ca}^{2+}$ ) imaging studies suggest that these two unique MSN populations could be uniformly engaged during movement and share a remarkably similar activity profile during normal locomotion<sup>12–15</sup>. These recent findings suggest that coordinated activity in D1 and D2 MSN populations supports normal voluntary movement, and that disrupting the balance of activity between these two pathways contributes to disease pathology<sup>11</sup>. The mechanisms underlying this coordination are less well understood, although they presumably include contributions of local interneurons.

In addition to MSNs, the dorsal striatum also contains multiple populations of interneurons, each of which represent only a small fraction of the total population of cells (<5% per type)<sup>7,16,17</sup>. Though few in number, each interneuron class has the potential to shape striatal activity and function through its innervation of the MSN projection network<sup>18,19</sup>. Two of the best-characterized striatal interneurons are the PV and CHI cell types. PVs are GABAergic and can provide a potent source of inhibition on the activity of nearby MSNs

to support motor control<sup>20–22</sup>. CHIs are a major source of striatal acetylcholine<sup>23,24</sup>. These extensively arborized cells can directly modulate the activity state of MSNs via muscarinic acetylcholine receptors expressed by both D1 and D2 populations of MSN<sup>25,26</sup>, and have likewise been implicated in normal control of motor output<sup>23,27,28</sup>.

The unique roles of PVs and CHIs in generating the MSN network dynamics that support movement remain unknown. Efforts to understand how sparsely distributed striatal interneurons interact with MSNs to support behavior have been hampered by a lack of experimental approaches that allow for the simultaneous monitoring of genetically defined interneuron populations in combination with large numbers of MSNs. To gain further insight into interneuron-MSN interactions in support of movement, we utilized a wide-field calcium imaging platform that enabled us to monitor and optogenetically manipulate interneurons, while simultaneously recording calcium dynamics in hundreds of surrounding MSNs in mice during voluntary locomotion. We find that PV and CHI interneuron types differ from one another, and from MSNs, in how they contribute to movement and how they regulate populations of MSN networks that guide behavior. PV interneurons best predict movement and reduce the level of MSN population activity in the dorsal striatum during movement events. CHIs, in contrast, have a more selective role in recruiting and synchronizing the activity of MSNs during movement to suppress or end a movement bout. Our combined evidence demonstrates the unique capacity of different classes of striatal interneurons to organize networks of MSNs in support of discrete aspects of voluntary locomotion.

## Results

**Simultaneous monitoring of MSN networks and PVs or CHIs during movement.** To simultaneously monitor activity in interneurons in conjunction with the surrounding population of dorsal striatal

<sup>1</sup>Department of Biomedical Engineering, Boston University, Boston, MA, USA. <sup>2</sup>Department of Neuroscience Icahn School of Medicine at Mt. Sinai, New York, NY, USA. <sup>3</sup>Department of Psychiatry Yale, School of Medicine, New Haven, CT, USA. <sup>4</sup>Department of Mathematics and Statistics Boston University, Boston, MA, USA. <sup>5</sup>Department of Electrical and Computer Engineering Boston University, Boston, MA, USA. <sup>6</sup>These authors contributed equally: Howard J. Gritton, William M. Howe, Michael F. Romano. \*e-mail: [xuehan@bu.edu](mailto:xuehan@bu.edu)

MSNs, PV-Cre and Chat-Cre mice were injected with AAV-Syn-GCaMP6f<sup>29</sup> to label all striatal neurons with the calcium activity indicator GCaMP6f. AAV-CAG-flex-tdTomato was also co-injected to allow us to label and identify GCaMP6f-expressing interneuron cell types (see Fig. 1a–c and Supplementary Fig. 1a for experimental timeline). Adeno-associated virus (AAV)-mediated flex-targeting allows for highly specific targeting of neuron classes, and we found that  $96.1 \pm 0.2\%$  of tdTomato cells were immunoreactive for PV antibody in PV-Cre mice (Supplementary Fig. 1b,c); and  $97.2 \pm 0.2\%$  of tdTomato cells were immunoreactive for Chat in Chat-Cre mice (Supplementary Fig. 1d,e) in the area below the imaging window. These numbers are consistent with measures reported previously for these specific transgenic mouse lines<sup>28,30</sup>. Importantly, we also found that <1% of cells co-expressed GCaMP and tdTomato but were immuno-negative for the corresponding Chat or PV antibody in Chat-Cre or PV-Cre mice, respectively, demonstrating selectivity.

Calcium responses for the three populations of cells in our experiments were recorded as mice ran freely on a spherical treadmill while tracking movement (Fig. 1a). Animals were positioned and imaged underneath a custom microscope equipped with a scientific complementary metal oxide semiconductor camera and imaged at  $10\times$  magnification (Fig. 1b). This yielded an imaging field of view of  $1.343 \times 1.343 \text{ mm}^2$  with each pixel corresponding to  $1.312 \times 1.312 \mu\text{m}^2$ , allowing in excess of 100 pixels to contribute to a single cell. GCaMP6f excitation was accomplished with a 460 nm LED, and tdTomato excitation with a 567 nm LED (Fig. 1b; for a complete description of the labeling, region of interest (ROI) identification and motion acquisition procedure see Supplementary Methods). As shown in Fig. 1c, this approach allowed us to monitor activity in genetically defined interneurons (CHIs:  $n = 5.1 \pm 1.1$  cells per session, PV:  $n = 4.4 \pm 0.8$ , mean  $\pm$  s.e.m.) in combination with large numbers of surrounding neurons ( $281.6 \pm 34.2$ , cells per session, mean  $\pm$  s.e.m.). Because the vast majority of striatal cells are MSNs (~95%), all GCaMP-positive and tdTomato-negative cells were treated as MSNs for the purpose of analysis (see Supplementary Methods for full description of dual-labeling approach and analysis). All statistical tests are reported in the corresponding figure legends and are corrected for multiple comparisons. A complete description of all tests and statistical models can be found in Supplementary Methods and the Reporting Summary.

**Striatal activity during locomotion.** We found that bulk striatal fluorescence (averaged activity across all cells) increased during periods of movement (high speed) and decreased during periods of no or low movement (low speed, Fig. 1d,e and Supplementary Video 1). For this reason, we focused our analyses around the time of movement onsets as well as peaks in velocity. In a typical 10 min recording session, 15–20 such locomotion events occurred (Chat-Cre mice,  $20.1 \pm 4.1$  onset events,  $n = 6$  mice; PV-Cre mice,  $14.9 \pm 3.0$ ,  $n = 6$  mice; mean  $\pm$  s.e.m.), with the average period of high movement velocity lasting  $5.1 \pm 0.1$  s (mean  $\pm$  s.e.m.). Individual MSN calcium events showed a sharp increase and an exponential decay (see Fig. 2a(top), for representative traces). Overall, calcium events were most frequent in MSNs of the three neuron types (Fig. 2b), and had the greatest amplitude (Supplementary Fig. 2a). Similar to recent imaging experiments in genetically defined populations of D1 and D2 MSNs, we found that the vast majority of MSNs exhibited a sharp increase in fluorescence at movement onset (Fig. 2d), although we did detect a proportion of MSNs that were either negatively (21.4%), or non-modulated (24.2%), by movement (Supplementary Fig. 3). As a population, MSN fluorescence rose coincident with movement onset (Fig. 2d–e), peaked coincident with maximum velocity (Fig. 2f,g) and then declined as movement slowed (Fig. 1d,e).

Calcium events in PV cells were slow to rise and long lasting (Fig. 2a(middle),c, Supplementary Fig. 2b,c and Supplementary

Video 2), consistent with calcium responses previously noted in PV neurons from cortical regions<sup>31</sup>. Like MSNs, PVs overwhelmingly exhibited increases in fluorescence around motion onset (Fig. 2d,e) while only 13.9% of the PV population was negatively modulated at movement onset (see Supplementary Figs. 3c and 4 for a full characterization of positively modulated PVs and the small subset of negatively modulated PVs). The increase in PV activity preceded MSNs by  $523.1 \pm 304.3$  ms (mean  $\pm$  s.e.m.;  $n = 13$  sessions, Fig. 2d; see Supplementary Figs. 5 and 6 for individual examples and Supplementary Methods for details). Indeed, PV cells also showed the highest proportion of neurons positively modulated in the 500 ms before movement onset (Supplementary Fig. 2h), providing further evidence for a rise in PV activity preceding motion onset and MSN activity. Additional analyses showed that in the 1.5 s following a calcium event in the PV population, calcium events were uniquely associated with a positive change in velocity (Fig. 2h and Supplementary Fig. 2i).

Calcium events in CHIs had event rates across periods of movement similar to PVs (Fig. 2b), and had the smallest AUC of all neuron classes (Fig. 2a(bottom),c), despite having rise times and event widths similar to those of MSNs (Supplementary Fig. 2b,c). As a population, CHIs showed a modest, but not statistically significant, increase in fluorescence at motion onset (Fig. 2d,e). Rather, CHI population fluorescence reached maximum intensity approximately 2 s after peak velocity (Fig. 2f,g and Supplementary Video 3). Analysis of changes in movement speed following CHI calcium events further indicated that speed dramatically declined following CHI calcium events (Fig. 2h and Supplementary Fig. 2i).

Further analyses indicated that CHIs were unique amongst the three cell types in that equal numbers of cells were positively (43.1%) or negatively (37.3%) modulated by motion onset, which presumably contributed to the small change in CHI population fluorescence described above (see also Supplementary Fig. 3c). The fluorescence of positively modulated CHIs peaked around maximum velocity (Supplementary Fig. 7c,d), similar to that in MSNs. In contrast, negatively modulated CHIs exhibited increased fluorescence 2 s after maximum velocity (Supplementary Fig. 7c); the same trend was observed when we considered the CHI population as a whole and as described above (Fig. 2f,g). Analysis of speed following calcium events in either positively or negatively modulated CHIs revealed that both populations were followed by similar reductions in speed in the 2 s following CHI events (Supplementary Fig. 7h). Thus while the two CHI populations became active at different time points in the movement sequence, each population was active before reductions in movement.

**Distinct causal roles for PV and CHI interneurons in movement.** In our correlative analysis described above, PV neurons homogeneously become active before movement bouts, perhaps providing a unified signal to increase the vigor or specificity of future locomotion. CHIs, while more heterogeneous than PVs or MSNs, as a population become active after peaks in velocity, and calcium events in CHIs were followed by reductions in speed. If each interneuron type is causing rather than tracking these changes in movement speed, manipulation of their activity should impact motor output. To test this hypothesis, we used optogenetics to control activation of PVs and CHIs while simultaneously recording locomotion and neuronal activity from MSN and interneuron populations. Specifically, the red-shifted, light-activated channelrhodopsin Chrimson<sup>32</sup> was expressed in PV or CHI interneurons using AAV-flex-Chrimson in PV-Cre or Chat-Cre mice. GCaMP6f was expressed in all striatal neurons as above using AAV-Syn-GCaMP6f. Mice were allowed to run freely on the spherical treadmill, while sparse periods (100 frames every ~6 s) of optogenetic stimulation occurred at random every 25–55 s (see Fig. 3a and Supplementary Methods).

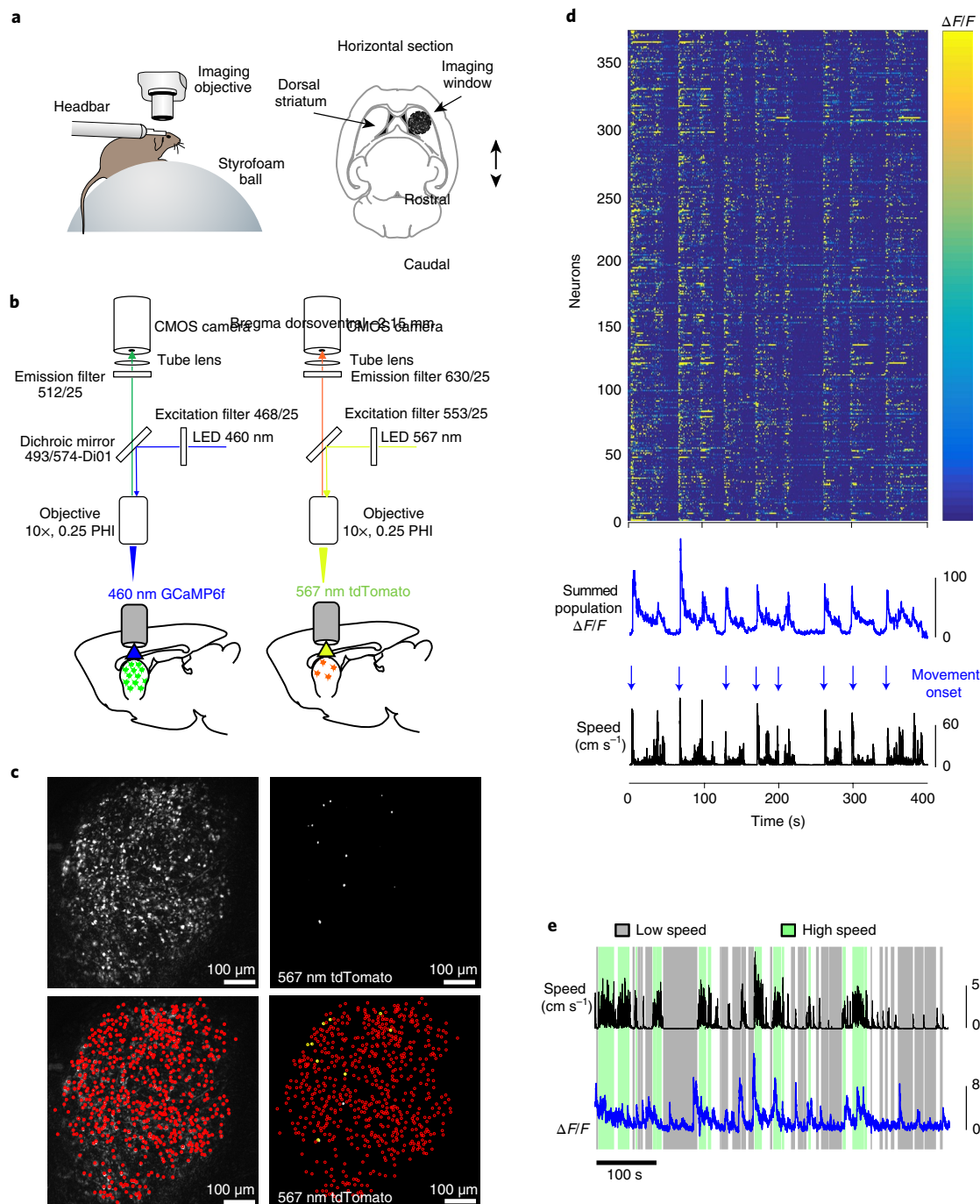


**Fig. 1 | Experimental framework and imaging protocol.** **a**, Left: schematic of behavioral set-up, showing a head-fixed mouse under the imaging scope positioned on a spherical treadmill. The animal's position and movement were simultaneously acquired along with calcium imaging data. Right: anatomical schematic showing placement of the imaging window for striatal recording. **b**, Imaging protocol. Recording sessions began with calcium imaging of GCaMP6f in the dorsal striatum using a 460 nm light-emitting diode (LED) (left), followed by tdTomato imaging with a 567 nm LED (right). **c**, Wide-field images from each recording condition described in **b** from a PV-Cre mouse. Top left: maximum-minimum pixel intensity map of GCaMP6f fluorescence across all frames. Bottom left: same GCaMP6f image overlaid with manually identified individual GCaMP6f-expressing cells (red circles). Top right: tdTomato fluorescence, with maximum pixel intensity map across all frames. Bottom right: same tdTomato image overlaid with identified GCaMP6f-expressing cells (yellow circles indicate cells co-expressing GCaMP6f and tdTomato). Recording sessions yielded a large total number of neurons ( $n = 281.6 \pm 34.2$ , mean  $\pm$  s.e.m. across 28 recording sessions) with a substantially smaller number of interneuron cell types (CHIs:  $n = 5.1 \pm 1.1$  cells per session, 10 sessions in 6 animals; PV:  $n = 4.4 \pm 0.8$ , mean  $\pm$  s.e.m. across 18 sessions in 6 animals). **d**, Color map showing GCaMP6f activity from 375 neurons (371 MSNs and 4 PVs) recorded during a representative 10 min imaging session from a PV-Cre animal. Bottom: summed population GCaMP6f fluorescence (blue, top) and linear velocity (speed, black) shown below the color map. Arrows indicate movement onsets (blue). Movement onsets and offsets were determined based on changes in movement speed thresholded independently (see Supplementary Methods). **e**, Extracted movement speed (black) and summed population GCaMP6f fluorescence of all neurons (blue curve, summed from 544 MSNs and 3 CHIs) from a representative Chat-Cre animal. Highlighting indicates periods of sustained high movement speed (green;  $> 5 \text{ cm s}^{-1}$  sustained) or low movement speed (gray;  $< 1 \text{ cm s}^{-1}$  sustained; see Supplementary Methods for details).

In PV-Cre mice, if optogenetic stimulation occurred when a mouse was already moving there was no impact on speed, although stimulation did introduce a transient change in side-to-side directional movement on the spherical treadmill, similar to that seen during endogenous PV events (see Supplementary Methods, Supplementary Fig. 8a,b and Supplementary Video 4). Surprisingly, when optogenetic stimulation occurred when animals were at rest, we found that it was sufficient to trigger a transition to movement (Fig. 3c). PV-triggered movement bouts plateaued ~1–1.5 s after laser onset, consistent with the enhanced period of motor output witnessed during endogenous PV events (Fig. 2h and Supplementary Fig. 2i). Importantly, the same laser stimulation protocol had no impact on behavior in PV-Cre control mice expressing only tdTomato (without Chrimson), or in Chat-Cre mice expressing Chrimson or tdTomato. Taken together, these results demonstrate that endogenous PV interneuron activity precedes motion onset and that their activation is sufficient to promote movement during periods of inactivity. Furthermore, our predictions regarding unique roles for each interneuron class in modulating behavior, based on the timing of calcium events from each cell class during voluntary movement, were confirmed by optogenetic manipulation of CHIs and PVs.

Consistent with our calcium imaging analysis of CHIs, optogenetic stimulation of these cells was sufficient to cause the animal to reduce ongoing movement (Fig. 3b) without altering direction (Supplementary Fig. 8). This effect was robust, and statistically significant, when averaged across all optogenetic stimulation events (Fig. 3b). Furthermore, if CHI stimulation occurred when the mouse was at rest, it did not trigger new movement (Fig. 3c). The same laser stimulation protocol had no impact on behavior in Chat-Cre control mice expressing only tdTomato in CHIs. The optogenetic results, combined with those from calcium imaging from endogenous activity in the CHIs described above, suggest that CHIs

function to reduce velocity or terminate ongoing bouts of locomotion (Fig. 3b and Supplementary Video 5).

**Characterization of coordinated MSN and interneuron activity.** Similar to other recent reports<sup>12,14</sup>, we found that calcium dynamics in cells adjacent to one another (within 100 μm) tended to be more correlated than those further away (Fig. 4a,e). Further, we found that correlations in fluorescence among cells varied by behavioral state (moving or at rest) and increased dramatically during periods of high-speed movement (Fig. 4b), presumably due to the increase in calcium event rate observed in all neuron types described above (Fig. 2b). Finally, this effect of movement state on correlated neural activity was strongest among pairs of neurons situated close to one another (Fig. 4c and Supplementary Fig. 9b), in line with recent findings of spatially organized clusters of dorsal striatal neurons emerging during locomotion<sup>12,14</sup>.

To get a sense of the correlational structure of calcium dynamics among neurons, and to control for the potential influence of changes in behavior on these relationships, we calculated asymmetric correlation coefficients<sup>12,33</sup> between pairs of identified MSNs and interneurons. The pairwise correlation between MSN pairs was low (correlation 0.08, Fig. 4d). When we considered the strength of MSN–MSN correlations by distance, we found, similar to recent studies, that the average correlation among MSNs decreased as the distance between cells increased (Fig. 4e), and only those in close proximity to one another were more correlated than chance. We further calculated the proportion of significantly correlated MSN pairs, and found that only a small subset of MSN pairs (~16%; Fig. 4f) exhibited such coordination. PVs, however, showed the highest degree of within-class correlation across the three classes (Fig. 4d,e), although only ~25% of PV cells (Fig. 4f) were significantly correlated with one another. Unlike MSNs, correlated calcium activity between pairs of PV cells was not impacted by distance

**Fig. 2 | Striatal population activity correlates with discrete aspects of movement.** **a**, Representative calcium events from the three types of neurons recorded; MSNs (top), PV cells (middle) and CHIs (bottom). **b**, Calcium event rates during high- versus low-speed periods. Event rates for all neurons increased during periods of high movement speed (sign-test, MSN: sign = 6,999, n = 7,518, 237 ties, P = 0; CHI: sign = 43, n = 47 neurons, 4 ties, P = 2.78 × 10<sup>-9</sup>; PV: sign = 66, n = 72 neurons, 7 ties, P = 7.26 × 10<sup>-14</sup>, across 28 sessions in 12 animals). **c**, Calcium event shape assessed as area under the curve (AUC), with PVs having the largest and CHIs the smallest waveforms (Kruskal-Wallis,  $\chi^2(2)$  = 37.3, P = 8.02 × 10<sup>-9</sup>, n<sub>MSN</sub> = 7,727, n<sub>PV</sub> = 78, n<sub>CHI</sub> = 50; mean ranks, MSN: 3.92 × 10<sup>3</sup>, PV: 5.36 × 10<sup>3</sup>, CHI: 3.13 × 10<sup>3</sup>; Tukey's honest significant difference (HSD) post hoc, PV versus MSN: P = 7.58 × 10<sup>-8</sup>, PV versus CHI: P = 1.80 × 10<sup>-7</sup>, MSN versus CHI: 0.038). This distinction was conserved during both high- and low-speed periods. MSNs also showed a small but significant increase in AUC between low- and high-speed movement periods, while PVs and CHIs were unchanged (sign-test, MSN: sign = 1,190, n = 1,813 neurons, 0 ties, P = 2.55 × 10<sup>-40</sup>; CHI: sign = 8, n = 11 neurons, 0 ties, P = 0.23; PV: sign = 5, n = 13 neurons, 0 ties, P = 0.58). \*P < 0.05, \*\*\*P < 0.001. **d**, Mean population fluorescence of each cell class relative to movement onset. Line-and-shaded regions indicate the mean ± s.e.m. **e**, Quantification of the change in fluorescence between the pre- and post-onset windows around movement onset. All cell classes showed an increase in mean fluorescence from pre-onset, except CHIs (change from pre-onset; sign-test, MSNs: sign = 2,540, n = 7,755 neurons from 12 mice, P = 1.60 × 10<sup>-202</sup>; CHIs: sign = 25, n = 51 neurons from 6 mice, P = 1; PVs: sign = 16, n = 79 neurons from 6 mice, P = 9.44 × 10<sup>-8</sup>). In PVs, the increase in fluorescence around motion onset began 523.1 ± 304.3 ms before that in MSNs. Line plots and error bars indicate the mean ± s.e.m. **f**, Mean population fluorescence of each cell class relative to peak velocity. Line-and-shaded regions indicate the mean ± s.e.m. **g**, Quantification of fluorescence across the peak velocity time period. MSNs and PV cells when compared to baseline (2 s before peak velocity) showed significantly elevated fluorescence in the 1 s before peak velocity and in each 1 s time bin following. CHIs did not show significantly higher fluorescence until after peak velocity, plateauing in the 1–2 s post-peak bin. Line plots and error bars indicate mean ± s.e.m. (mixed-effects model; ANOVA for interaction of cell type and time bin: F(10, 6.11 × 10<sup>6</sup>) = 9.52, P = 4.91 × 10<sup>-16</sup>; fluorescence for PVs at bin 1 (−1 to 0 s pre-peak): t(48,198) = 3.08, P = 0.00278 vs baseline; fluorescence for MSNs (−1 to 0 s pre-peak): t(6.00 × 10<sup>6</sup>) = 21.6, P = 3.34 × 10<sup>-103</sup> vs baseline, fluorescence for CHIs (0 to 1 s following peak velocity): t(59,244) = 2.93, P = 0.00428 vs baseline). **h**, Normalized change in movement speed centered on calcium events sorted by cell class. Line plots and error bars indicate mean ± s.e.m. Analysis revealed a significant interaction between time bin and cell type (mixed-effects model, ANOVA F(8, 39,260) = 3.61, P = 0.00034), so comparisons were broken down by cell type. CHI calcium events were followed by a significant decrease in speed compared with events from the other two cell types. Comparisons of time windows to baseline, 0–500 ms (CHIs: t(245) = −0.33, P = 0.81; PVs: t(385) = −0.42, P = 0.81; MSNs: t(38,630) = 5.0, P = 1.9 × 10<sup>-6</sup>); 500–1,000 ms (CHIs: t(245) = −2.0, P = 0.089; PVs: t(385) = 1.02, P = 0.52; MSNs: t(38,630) = −0.76, P = 0.59); 1,000–1,500 ms (CHIs: t(245) = −3.6, P = 9.2e-04; PVs: t(385) = 0.95, P = 0.52; MSNs: t(38,630) = −10.0, P = 9.1 × 10<sup>-23</sup>); 1,500–2,000 ms (CHIs: t(245) = −4.68, P < 0.001; PVs: t(385) = −0.19, P = 0.85; MSNs: t(38,630) = −18.4, P = 3.83 × 10<sup>-74</sup>); Benjamini-Hochberg corrected across all cell types and time bins (n = 12 comparisons; n<sub>MSN</sub> = 7,727, n<sub>CHI</sub> = 50 and n<sub>PV</sub> = 78). A total of 30 cells out of 7,855 did not produce an event that was included in this analysis (see Methods for details; MSN, n = 28 cells; PV, n = 1 cell; CHI, n = 1 cell). For all box plot figures, middle lines indicate the median; lower and upper edges of the box indicate quartiles below and above the median; and upper and lower whiskers indicate the points furthest from the median whose value did not exceed 1.5 times the first-to-third quartile range above the third quartile or below the first quartile. All sign-tests were two-sided.

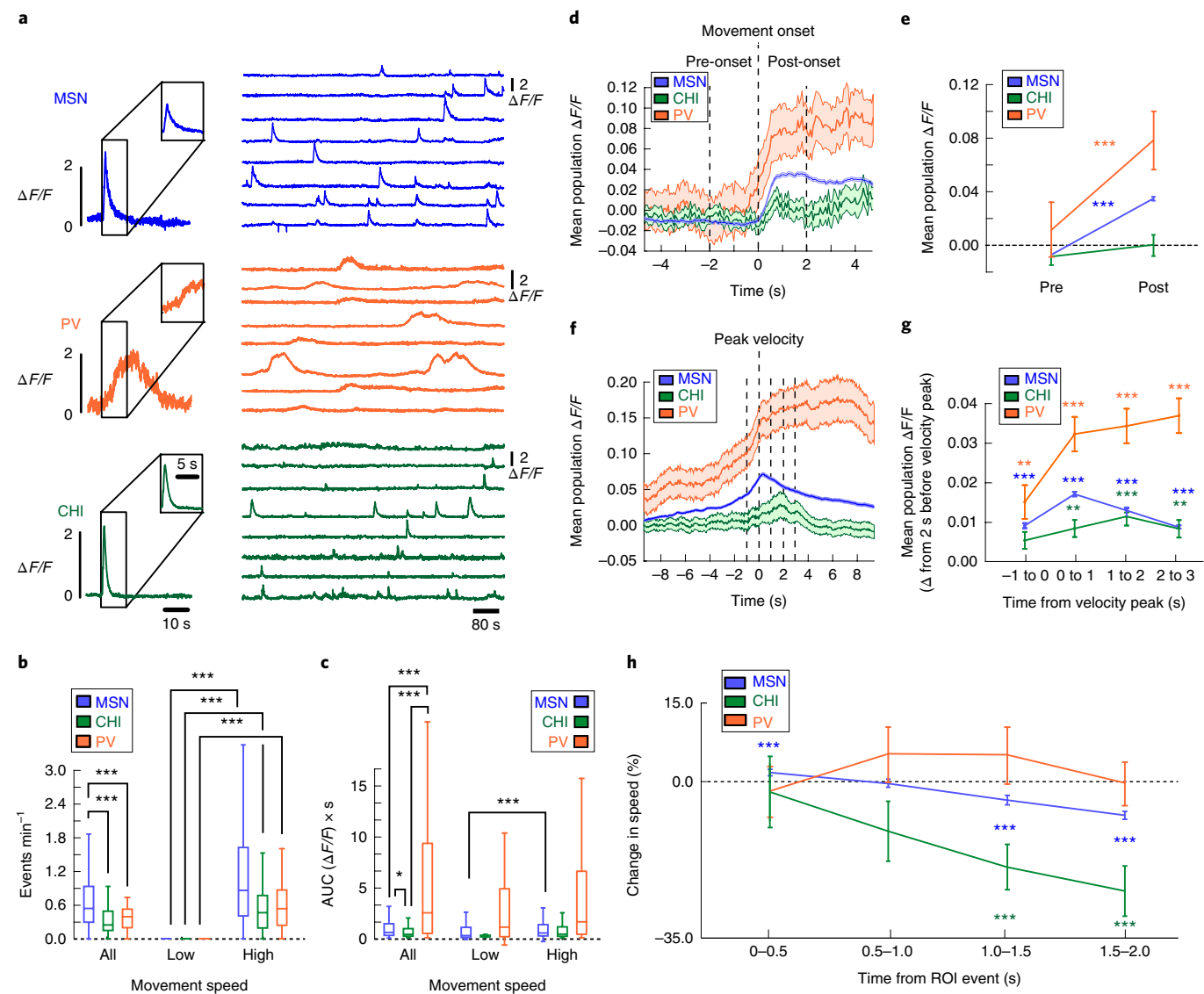
(Fig. 4e). In contrast, CHI pairs were characterized by the weakest within-class correlation and the fewest number of correlated pairs of the three neuron types (Fig. 4d–f). The strength of the correlation between CHIs, like PVs, did not vary by the distance between cells (Fig. 4e). Thus distance-dependent correlated activity appears to be a feature unique to MSN pairs during voluntary locomotion.

Lastly we considered coordinated activity between MSNs and interneurons (Fig. 5a). Across all interneuron–MSN combinations, the proportion of correlated cell pairs decreased with distance although this decline was sharpest for PV–MSN pairs (Fig. 5a, middle), as reflected by the median distance between correlated cells (Fig. 5b). In contrast, distance had a much lower influence on correlated CHI–MSN pairs (Fig. 5a, right), which were characterized by the largest median distance between related cell pairs (Fig. 5b). In concert, these findings are consistent with the prescribed roles of PV cells providing perisomatic inhibition to a local network of nearby MSNs<sup>22</sup>, whereas CHI interneurons appear to affect networks of MSNs over greater distances, perhaps via their extensive arborization<sup>23,34</sup>.

**PVs and CHIs differentially predict movement and MSN activity.** Having characterized neural activity surrounding movement, determined a causal role of interneuron activity in movement and defined the degree of correlated activity between neurons, we next

sought to determine how each interneuron population coordinates MSN activity to control movement. To this end, we first created linear statistical models and tested the capacity of calcium dynamics in interneurons to predict changes in global MSN population fluorescence. Because we found that population fluorescence in the striatum was highly correlated with both speed and rotation (see Supplementary Figs. 2d,g and 9), we considered both factors in our model. We found that the small number of PV cells recorded during a session was equivalent to the power of either speed or rotation in predicting MSN population fluorescence (Fig. 6a,b). Since both endogenous and optogenetically evoked PV activity also coincided with changes in movement onset, we further examined whether PV activity could be used as a predictor of speed. We found that the predictive power of the small population of PV neurons ( $n=4.6$ ), although slightly lower, was similar to that of the entire population of MSNs ( $n=244.2$  neurons per session, Fig. 6c,d).

In contrast to PVs, the population of CHIs ( $n=5.1$  neurons per session) were weak predictors of both MSN population activity (Fig. 6e,f) and velocity (Fig. 6g,h). Importantly, we used regression models because the strength of the prediction for individual neurons would not be affected by whether neurons are positively or negatively modulated by movement. However, given the heterogeneity of CHI responses to motion onset, we conducted additional analyses that



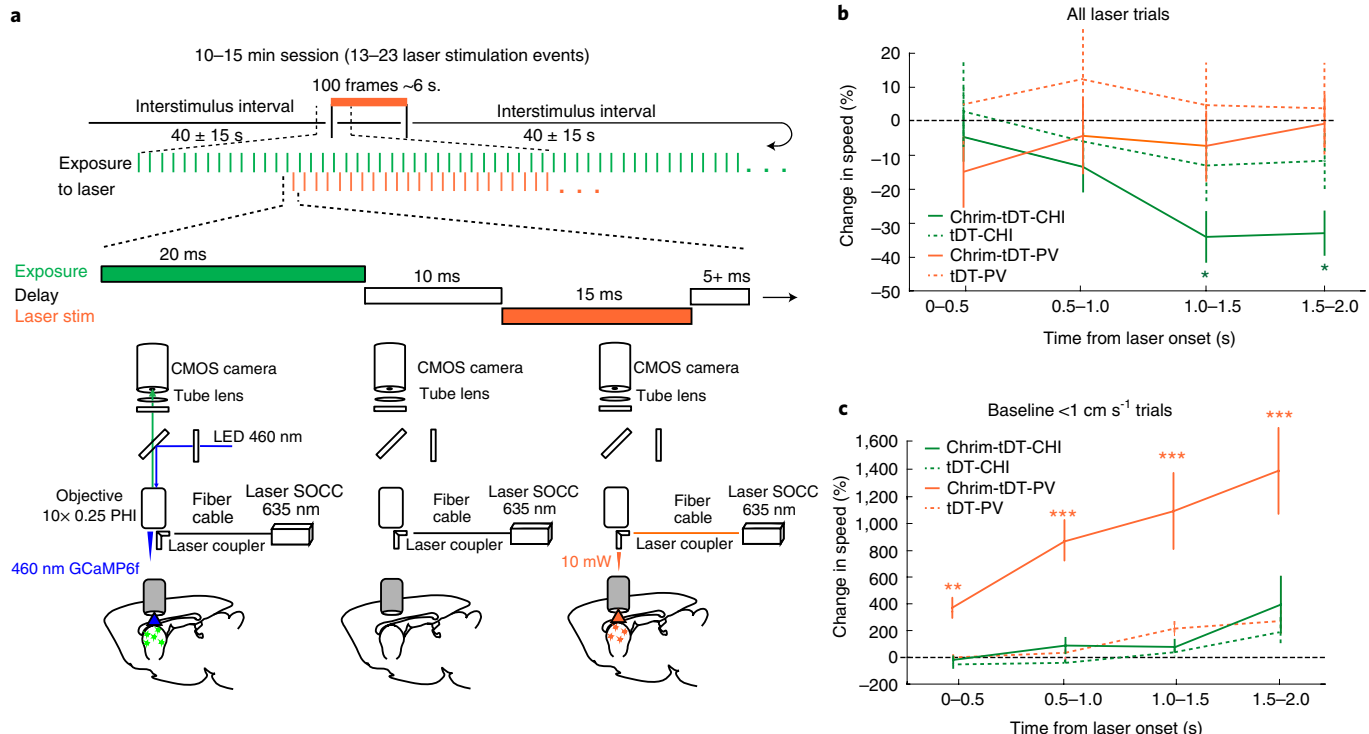


**Fig. 3 | Optogenetic stimulation of interneuron populations modulates movement.** **a**, Simultaneous optogenetic stimulation and imaging experimental design. Top: animals were imaged over 10–15 continuous minutes and received 13–23 trials of optogenetic stimulation with an ITI of  $40 \pm 15$  s. Each trial consisted of 100 laser stimulation pulses at 15 Hz. Red laser light was pulsed between GCaMP6f imaging frames. Bottom: cartoon depicting alternating GCaMP6f image acquisition and red laser light delivery for Chrimson activation through the imaging window across successive frames. **b**, Normalized change in movement speed at laser onset for PV-Chrimson and Chat-Chrimson mice for all trials ( $n=4$  PV-Chrimson mice, and  $n=4$  Chat-Chrimson mice, two sessions for each mouse). Line plots and error bars indicate mean  $\pm$  s.e.m. Significant reductions in speed coincided with laser onset only in Chat-Chrimson mice (mixed-effects model, ANOVA  $F(4, 645)=6.7, P<0.001$ ; comparisons of time windows 0–500 ms;  $t(645)=-0.91, P=0.36$ , 500–1,000 ms;  $t(645)=-1.8, P=0.11$ , 1,000–1,500 ms;  $t(645)=-3.8, P=6.20 \times 10^{-4}$ ; 1,500–2,000 ms,  $t(645)=-3.6, P=8.10 \times 10^{-4}$ ; \* $P<0.01$ , Benjamini-Hochberg corrected). This effect was not present in PV-Chrimson mice (mixed-effects model, ANOVA  $F(4, 575)=1.4, P=0.24$ ), or in control mice ( $n=4$  PV-tdTomato mice, and  $n=4$  Chat-tdTomato mice, two sessions for each mouse; PV-tdTomato mice: mixed-effects model, ANOVA  $F(4, 580)=6.0, P=0.60$ ; Chat-tdTomato mice: mixed-effects model, ANOVA  $F(4, 580)=2.2, P=0.07$ ). **c**, Normalized change in movement speed following laser onset for PV-Chrimson and Chat-Chrimson mice when stimulation occurred during periods of low movement. Line plots and error bars indicate mean  $\pm$  s.e.m. Laser stimulation increased movement only in PV-Chrimson mice (mixed-effects model, ANOVA  $F(4, 200)=5.4, P=4.00 \times 10^{-4}$ ; baseline versus time = 0–500 ms:  $t(200)=3.16, P=0.0018$ ; baseline versus time = 500–1,000 ms:  $t(200)=4.3, P=6.20 \times 10^{-5}$ ; baseline versus time = 1,000–1,500 ms:  $t(200)=3.6, P=6.00 \times 10^{-4}$ ; baseline versus time = 1,500–2,000 ms:  $t(200)=4.3, p=6.20 \times 10^{-5}$ ), but not in Chat-Chrimson mice (mixed-effects model, ANOVA  $F(4, 130)=1.7, P=0.15$ ) or in control mice (PV-tdTomato: mixed-effects model, ANOVA  $F(4, 170)=2.2, P=0.07$ ; Chat-tdTomato mice: mixed-effects model, ANOVA  $F(4, 150)=1.2, P=0.31$ ,  $n=4$  tdTomato mice, two sessions from each mouse). \* $P<0.05$ , \*\* $P<0.01$ , \*\*\* $P<0.001$ .

considered positively and negatively modulated CHI populations in isolation. We found that the positive and negative populations differed from one another in neither their predictive relationship toward MSN activity (Supplementary Fig. 7*i*, left) nor speed (Supplementary Fig. 7*i*, right). Thus, while CHI and PV neurons had similar representations in the total number of neurons across recording sessions, only PV neurons were prominent predictors of both instantaneous striatal bulk fluorescence and locomotor output.

**PVs and CHIs modulate movement through unique effects on MSN activity.** While the predictive modeling described above demonstrates the extent to which interneuron activity can forecast MSN calcium dynamics and movement, it does not provide information on whether MSN population dynamics are impacted by changes in PV or CHI activity. Therefore, using the deconvolved calcium fluorescence signal (see Supplementary Fig. 10 and Methods) to align calcium events in each population, we next assessed changes in activity within the population of MSNs when these coincided with PV or CHI events. Specifically, we compared MSN activity around

interneuron events to that observed by chance around other randomly selected MSN events. We found that on average, MSN population fluorescence was lower than chance when associated with a PV calcium event (Fig. 7*a*), suggesting that PV activity could contribute to a decrease in the MSN population response. In contrast, MSN population fluorescence was elevated when coincident with a CHI calcium event (Fig. 7*b*), suggesting that CHI activity may activate or recruit the MSN population.

Having revealed that interneuron activity coincides with changes in MSN fluorescence, we further considered whether this change in fluorescence was a result of changes in coincident activity between MSN pairs. Specifically, we quantified the incidence of MSNs exhibiting coincident calcium events when interneurons are active compared to what would be expected by chance (see Supplementary Methods for details). We found that MSN–MSN co-activity was reduced when aligned to PV events, relative to MSNs or CHIs (Fig. 7*c*). Thus the reduction in MSN fluorescence observed during PV activation was concomitant with a reduction in coincident events in the MSN population. When we performed the same analysis on the

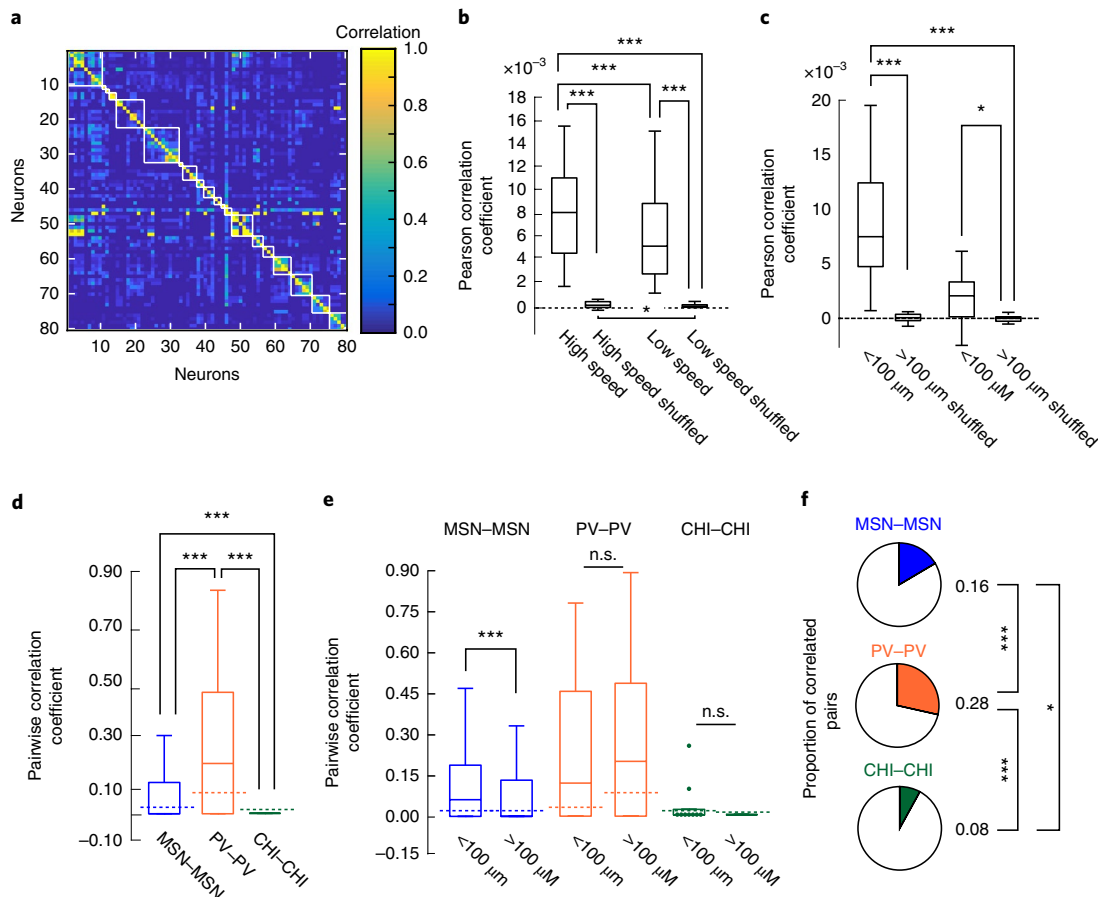


**Fig. 4 | Anatomical clustering and coordinated activity within each cell population.** **a**, Correlation matrix utilizing asymmetric correlation coefficients of 80 neurons from a randomly chosen recording session. White lines represent boundaries between unique neuron pairs less than 100 μm distant from one another. **b**, Box plots of pairwise Pearson correlation coefficients during periods of high and low speed from all animals. Correlation between neuron pairs increased with speed (sign-test, two-sided, sign = 24,  $P=1.80 \times 10^{-4}$ ,  $n=28$  sessions; high speed versus shuffled, sign = 28,  $P=7.45 \times 10^{-9}$ ; low speed versus shuffled, sign = 28,  $P=7.45 \times 10^{-9}$ , high speed shuffled versus low speed shuffled, sign = 21,  $n=28$  sessions,  $P=0.0125$ ). **c**, Difference in pairwise strength between periods of high and low movement sorted by anatomical distance across all cells from all sessions in all mice. The change in correlation strength was greatest between adjacent cells (all two-sided sign-tests, sign-test,  $<100 \mu\text{m}$  versus  $>100 \mu\text{m}$ ; sign = 26,  $P=3.03 \times 10^{-6}$ ,  $n=28$  sessions; sign-test,  $<100 \mu\text{m}$  versus  $<100 \mu\text{m}$  shuffled, sign = 27,  $P=2.16 \times 10^{-7}$ ; sign-test,  $>100 \mu\text{m}$  versus  $>100 \mu\text{m}$  shuffled, sign = 21,  $P=0.0125$ ). **d**, Pairwise asymmetric correlation between the same cell types. Dotted lines indicate median of averaged correlation coefficients for within-cell type shuffled data. PV cells showed the highest correlation coefficient values (Kruskal-Wallis,  $X^2(2)=1.5 \times 10^2$ ,  $P=7.69 \times 10^{-33}$ , mean ranks, MSN:  $7.46 \times 10^5$ , PV:  $1.03 \times 10^6$ , CHI:  $5.99 \times 10^5$ ; Tukey's HSD post hoc, MSN-MSN versus CHI-CHI:  $P=8.80 \times 10^{-6}$ ; MSN-MSN versus PV-PV:  $P=9.56 \times 10^{-10}$ ; PV-PV versus CHI-CHI:  $P=9.56 \times 10^{-10}$ ), and were correlated above that expected by chance based on within-neuron-type shuffled data (sign-test, sign = 146,  $n=241$  PV-PV pairs,  $P=0.0013$ ). MSN-MSN pairs and CHI-CHI pairs were not significantly different from shuffled data. **e**, Population box plots showing asymmetric pairwise correlation of each cell type across all 28 recording sessions sorted by anatomical distance. Dotted lines indicate median of averaged correlation coefficients for shuffled data for each cell pair. Pairs of MSNs in close proximity ( $<100 \mu\text{m}$ ) are more correlated than those further apart. Unlike MSN pairs, PV pairs and CHI pairs were not modulated by distance (effect of distance; two-sided Wilcoxon rank-sum, MSN-MSN pairs,  $w=5.3 \times 10^{10}$ ,  $n_{<100}=62,895$ ,  $n_{>100}=1,429,304$ ,  $P=0$ ; PV-PV pairs,  $w=1,955$ ,  $n_{<100}=17$ ,  $n_{>100}=224$ ,  $P=0.71$ ; CHI-CHI pairs,  $w=684$ ,  $n_{<100}=9$ ,  $n_{>100}=143$ ,  $P=1.0$ ). As expected, only MSN pairs within 100 μm were more correlated than chance based on within-neuron-class shuffled data (sign-test, MSN-MSN pairs  $<100 \mu\text{m}$ , sign = 32,864,  $n=62,894$  MSN-MSN pairs, ties = 1,  $P=1.37 \times 10^{-29}$ ; PV-PV pairs  $>100 \mu\text{m}$ , sign = 137,  $n=224$  PV-PV pairs,  $P=0.0011$ ). All other comparisons were not different from chance based on shuffled data. **f**, Population pie charts showing the number of significantly correlated pairs of neurons above those expected by chance from shuffled data, sorted by cell type. A greater proportion of PV cell pairs was correlated than MSN pairs, and both were more correlated than CHI pairs (MSNs versus CHIs:  $X^2(1)=7.2$ ,  $P=0.022$ ; PVs versus CHIs:  $X^2(1)=26.3$ ,  $P=8.72 \times 10^{-7}$ ; MSN-MSN: 238,293/1,501,649 pairs, PV-PV: 68/244 pairs, CHI-CHI: 13/160 pairs). For all box plot figures, middle lines indicate the median; lower and upper edges of the box indicate quartiles below and above the median; and upper and lower whiskers indicate the points furthest from the median whose value did not exceed 1.5 times the first-to-third quartile range above the third quartile or below the first quartile.

optogenetic stimulation sessions, we found that PV activation also reduced MSN-MSN co-activity during laser-on periods when compared to CHI stimulation or endogenous MSN-MSN co-activity (Fig. 7d,e). Further MSN population analysis revealed that optogenetic stimulation of PVs did not universally inhibit MSNs, but

rather produced heterogeneous changes in MSN activity, including increases in activity in subpopulations of MSNs (Supplementary Fig. 4g). The combined evidence suggests a model whereby PVs support specific movement plans by determining which MSNs are currently active<sup>35</sup>.

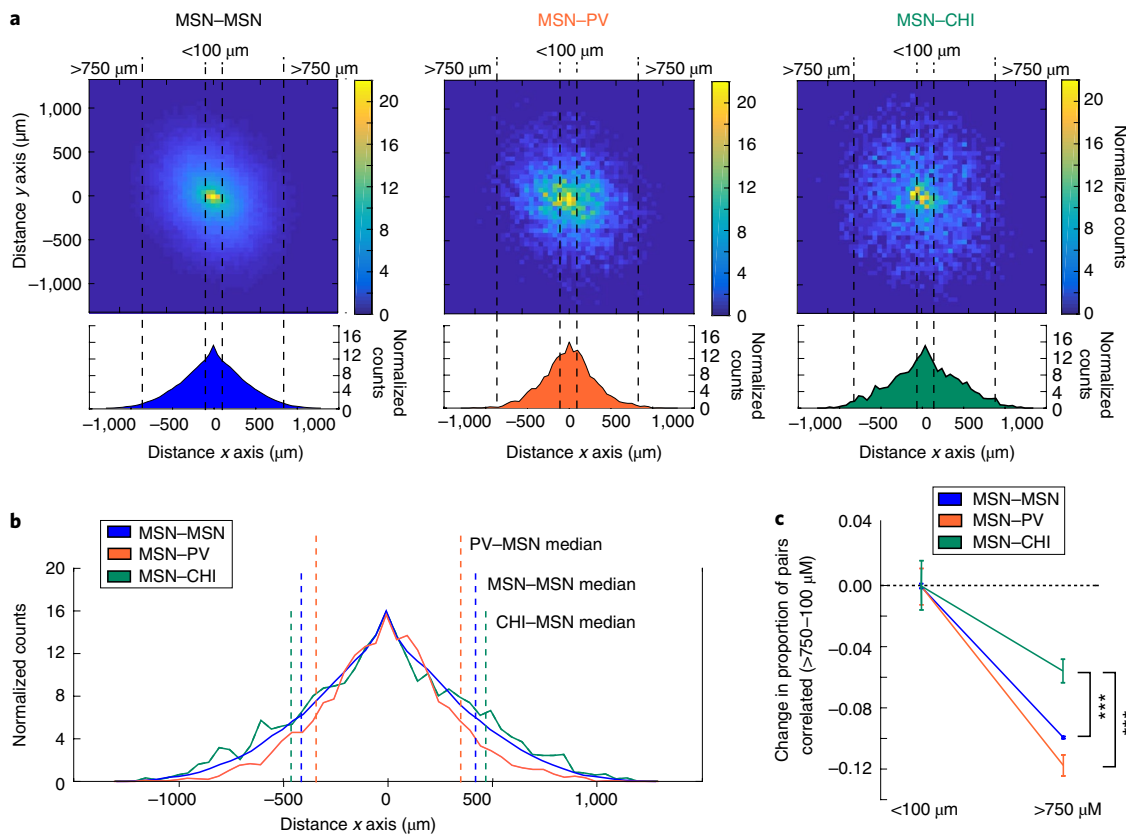


**Fig. 5 | Coordinated activity between interneurons and MSNs by anatomical distance.** **a**, Population color maps from all sessions in all animals showing significantly correlated cell pairs sorted by distance. Density distributions from above in the x axis are shown below. MSN-MSN cell pairs (left) and MSN-interneuron cell pairs (PV, middle; CHI, right). MSN-CHI cell pairs are correlated over greater distances than MSN-MSN pairs, and MSN-PV are correlated over smaller distances than MSN-MSN pairs (MSN-MSN median = 411 μms, MSN-PV: 343 μm, MSN-CHI: 448 μm; Kruskal-Wallis,  $\chi^2(2) = 303$ ,  $n_{\text{MSN-MSN}} = 238,293$ ,  $n_{\text{MSN-PV}} = 4,028$ ,  $n_{\text{MSN-CHI}} = 2,686$ ,  $P = 1.87 \times 10^{-66}$ ; mean ranks: MSN-MSN:  $1.23 \times 10^5$ , MSN-PV:  $1.04 \times 10^5$ , MSN-CHI:  $1.31 \times 10^5$ ; Tukey's HSD post hoc, MSN-PV versus MSN-MSN:  $P = 9.56 \times 10^{-10}$ , MSN-PV versus MSN-CHI:  $P = 9.56 \times 10^{-10}$ , MSN-MSN versus MSN-CHI:  $P = 9.53 \times 10^{-9}$ ).

**b**, Population density distributions showing the x-direction from **a** for all cell types superimposed. The median value distance value from **a** has been plotted for reference on the x-direction plot. **c**, Measure of the expected values between the proportion of significantly correlated pairs for populations MSN-MSN, MSN-PV and MSN-CHI for those separated by a distance of >750 μm versus <100 μm. Data >750 μm are plotted relative to <100 μm values. For all interneuron-MSN combinations, the proportion of correlated pairs decreased as the distance between cells increased, though the decrease in CHI-MSN pairs was more modest than that seen for PV-MSN or MSN-MSN pairs. Center indicates expected value, error bars are  $\pm$ s.e. (generalized linear model, binomial family with identity link function; 274,589 total observations; Benjamini-Hochberg-corrected P values of interaction terms (two-sided t-tests), MSN-MSN versus MSN-CHI:  $t(274, 583) = 4.07$ ,  $P = 1.39 \times 10^{-4}$ ; MSN-MSN versus MSN-PV:  $t(274, 583) = -0.56$ ,  $P = 0.573$ ; MSN-PV versus MSN-CHI:  $t(274, 583) = -3.42$ ,  $P = 9.53 \times 10^{-4}$ ). All comparisons are made using pairwise data across 28 sessions in 12 animals (6 PV-Cre and 6 Chat-Cre). \* $P < 0.05$ , \*\* $P < 0.001$ .

In contrast, CHI events appeared to have had the opposite effect on the MSN population and were associated with increased MSN-MSN co-activity, suggesting that CHIs may play a role in enhancing such coincident activity in the population of MSNs (Fig. 7c). In line with these observations, optogenetic stimulation of CHIs increased both MSN fluorescence (Supplementary Fig. 11b) and the probability of both MSN activity (Supplementary Fig. 11f) and MSN-MSN co-activity during laser-on periods (Fig. 7d,e). To explore whether CHI-mediated enhancement of MSN-MSN co-activity might represent a mechanism underlying the capacity of CHIs to reduce ongoing movement, we analyzed motor output during peaks in MSN-MSN co-activity. We found that these peaks were followed by significant reductions in motor output (Fig. 7f), mirroring the reductions in velocity seen in association with endogenous CHI activity (Fig. 2h) or optogenetic stimulation of CHIs (Fig. 3b).

Together, our data support distinct and dissociable functions of PVs and CHIs in modulating MSNs to support voluntary movement. Optogenetic stimulation of PVs increased future movement and, given their superior capacity in predicting MSN population

fluorescence and speed, our data strongly support a specific role for PVs in refining the populations of MSNs recruited during the execution of planned movement. In contrast, although CHIs are poor predictors of instantaneous speed or MSN population activity, CHI activation is sufficient to reduce movement. This effect was also accompanied by enhanced coordinated activity within the MSN population. Such CHI-mediated MSN coordination represents a unique and previously unknown means by which striatal networks act to terminate ongoing movement sequences.

## Discussion

To begin to understand how PVs and CHIs modulate striatal MSN activity in support of voluntary movement, we developed a large-scale, two-color imaging assay that enabled us to observe the activity of both interneurons and hundreds of surrounding MSNs in mice as they ran on a spherical treadmill. Because recent studies employing optical imaging to monitor activity in genetically defined D1 versus D2 MSNs did not differentiate these cell types from one another in healthy mice during spontaneous locomotion<sup>11–15</sup>, we

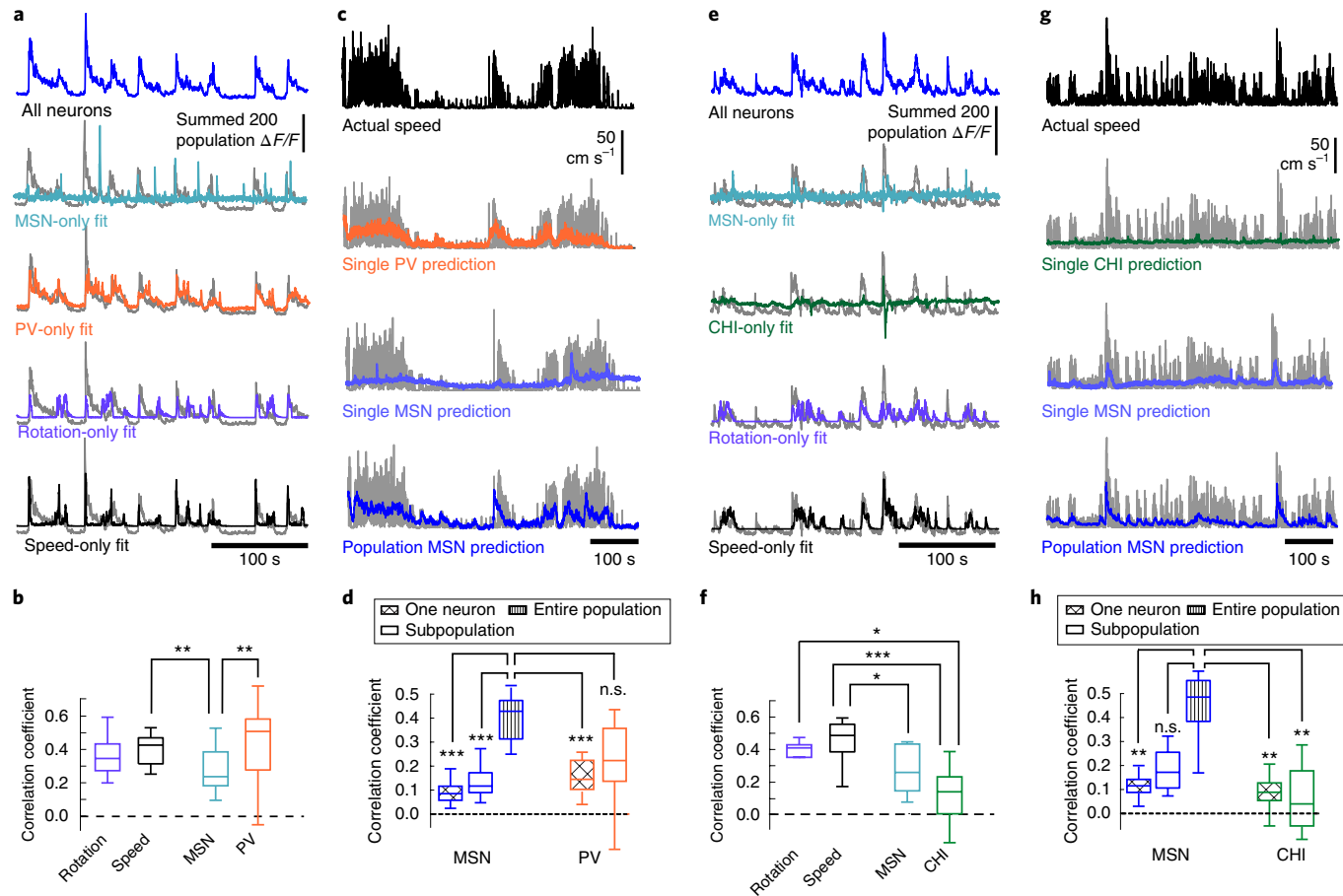


**Fig. 6 | PVs, but not CHIs, are strong predictors of speed and MSN population activity.** **a**, Striatal population fluorescence (blue, top; gray, bottom four) and predicted fluorescence based on PV activity (orange) or an equivalent number of MSNs (teal) from a representative PV-Cre mouse. **b**, Quantification across all PV-Cre mice. Predictions of population fluorescence were compared to that derived from using motor output (rotation, purple; speed, black). PV calcium dynamics were better predictors than that of an equivalent number of MSNs, and similar to speed and rotation; Friedman test,  $X^2(3)=18.0$ ,  $P=4.47 \times 10^{-4}$ ,  $n=17$  sessions in 6 mice; mean ranks, speed 2.94, rotation 2.53, PV 3.12, MSN 1.41; post hoc Tukey's HSD, speed versus PV:  $P=1.0$ , rotation versus PV:  $P=0.54$ , PV versus MSNs:  $P=6.8 \times 10^{-4}$ . **c**, Actual speed and predicted speed based on PV cell activity or MSN activity for a representative PV mouse. Experimentally measured speed is plotted in black (top) and gray (bottom three), compared with predicted velocity using the activity of a single PV (orange), a single MSN (light blue) and the full MSNs population activity (dark blue). **d**, Quantification of population predictor performance across all PV-Cre mice. The ability of the full PV population from each recording session to predict speed was also compared to an equivalent number of MSNs ( $n=4.6 \pm 0.86$  PV cells across 17 sessions with at least one PV cell, mean  $\pm$  s.e.m.), referred to as 'subpopulation'. The activity of a single PV was a significant predictor of speed, and the small population of PVs has equal predicting power speed to the entire population of MSNs (Friedman test,  $X^2(4)=50.1$ ,  $P=3.51 \times 10^{-10}$ ; mean ranks, single MSN: 1.32, multiple MSN: 2.56, all MSN: 4.94, multiple PV: 3.56, single PV: 2.62,  $n=17$  sessions; Tukey's HSD post hoc, MSN all-MSN single:  $P=1.01 \times 10^{-8}$ ; MSN all-MSN subgroup:  $P=9.12 \times 10^{-5}$ , MSN all-PV all:  $P=0.076$ ). **e,f**, Same as **a,b** but for CHI neurons in Chat-Cre mice. Unlike PVs, CHI calcium dynamics were poor predictors of population fluorescence. Friedman test,  $X^2(3)=24$ ,  $P=2.50 \times 10^{-5}$ ,  $n=10$  sessions in 6 mice; mean ranks, speed 3.9, rotation 2.7, CHI 1.1, MSN 2.3; Tukey's HSD post hoc, speed versus CHI:  $P=7.36 \times 10^{-6}$ , rotation versus CHI:  $P=0.029$ , MSN versus CHI:  $P=0.16$ . **g,h**, Same as **c,d** but from a representative Chat-Cre mouse (**g**) and predictor performance quantification for all Chat-Cre mice (**h**). Actual speed is shown in black or gray. Predicted speed based on the activity of a single CHI neuron in green, a single MSN in light blue and population MSNs in dark blue. Subpopulations represent a number of MSNs equivalent to the full CHI population from each recording session ( $n=5.1 \pm 1.1$  CHIs across all recording sessions, mean  $\pm$  s.e.m.). CHIs were weak predictors of speed, and using the full population of CHI cells did not significantly improve the predictive power over a single CHI (Friedman test,  $X^2(4)=20.8$ ,  $P=3.44 \times 10^{-4}$ ; mean ranks, single MSN: 2.5, multiple MSN: 3.4, all MSN: 4.8, multiple CHI: 2.2, single CHI: 2.1,  $n=10$  sessions in 6 mice; Tukey's HSD post hoc, MSN all-MSN single:  $P=0.0090$ , MSN all-CHI single:  $P=0.0011$ , MSN all-CHI all:  $P=0.0019$ , CHI all-CHI single:  $P=1.0$ ). \* $P<0.05$ , \*\* $P<0.01$ , \*\*\* $P<0.001$ . For all box plot figures, middle lines indicate the median; lower and upper edges of the box indicate quartiles below and above the median; and upper and lower whiskers indicate the points furthest from the median whose value did not exceed 1.5 times the first-to-third quartile range above the third quartile or below the first quartile.

considered MSN populations as a single population in our analyses. Distinctions between D1 and D2 MSN activity have been described for goal-directed versus habitual behaviors<sup>36,37</sup>. However, our data, in the context of other recent imaging studies<sup>11–15</sup>, suggest that these distinctions probably reflect striatal network remodeling inherent in learning particular goal-directed action sequences. Thus, while our studies specifically sought to characterize the role of two major

interneuron populations in modulating general MSN activity and voluntary movement, future studies could uncover distinct influences of PV and CHI cells on direct or indirect pathway MSNs for different behaviors<sup>30,38</sup>.

We found evidence that both PVs and CHIs have activity-behavior relationships that are distinct from MSNs. While MSNs are topographically organized by their relationship to motor output

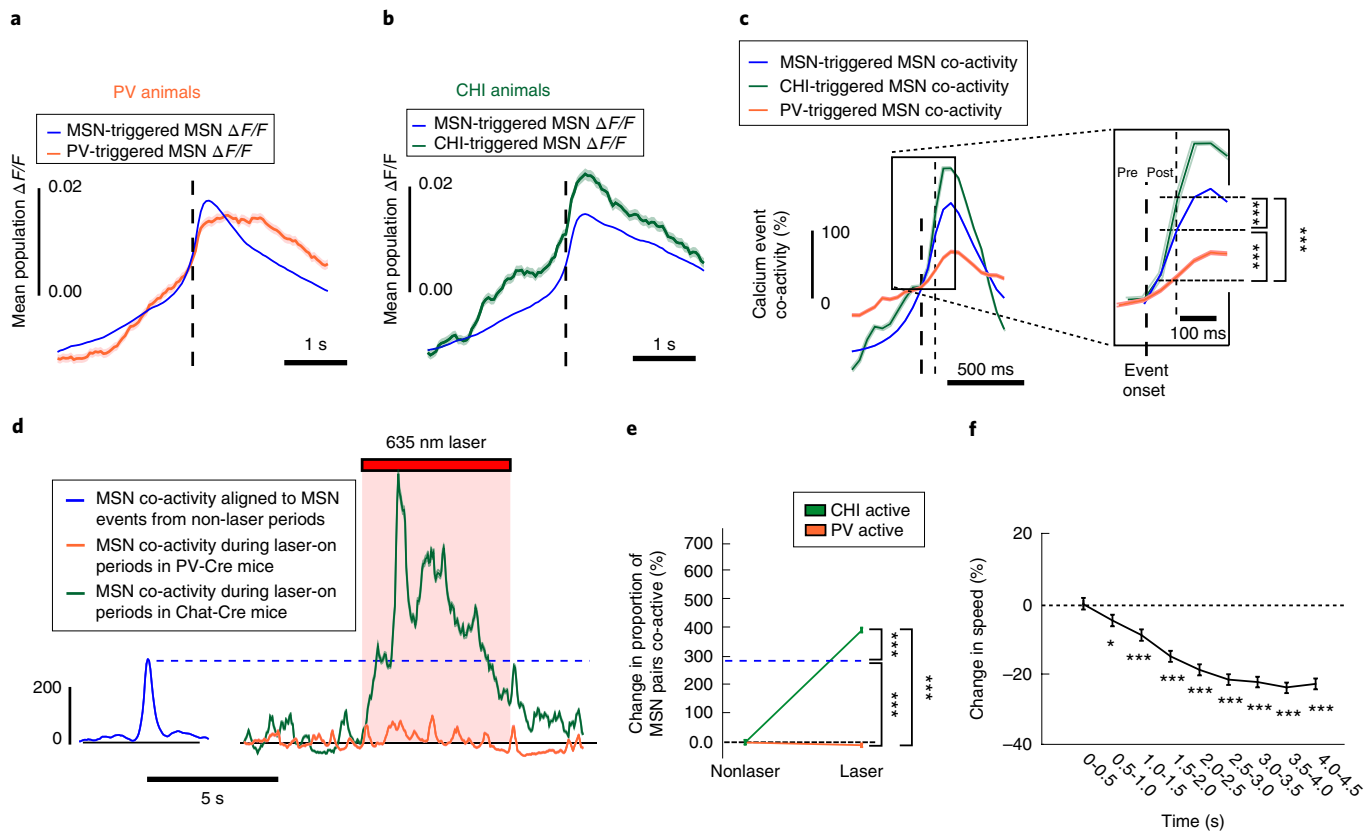


**Fig. 7 | Interneurons regulate MSN activity and movement state.** **a**, MSN population fluorescence aligned to all PV calcium event onsets (orange) versus MSN calcium event onset (blue) from all PV-Cre animals. MSN population peak fluorescence was significantly reduced in the 500 ms following a PV calcium event (PV post-event: rank-sum test, two-sided, rank-sum =  $2.43 \times 10^{12}$ ,  $n_{PV} = 237,528$  event-neurons,  $n_{MSN} = 20,289,773$  event-neurons, across all 6 PV animals and 18 sessions,  $P = 1.48 \times 10^{-6}$ ), in comparison to a MSN calcium event (blue). Plots are mean  $\pm$  s.e.m. **b**, Same as **a** but for Chat-Cre animals. MSN peak population fluorescence was significantly elevated in the 500 ms following a CHI calcium event (green, Chat-Cre post-event: two-sided, rank-sum test, rank-sum =  $1.73 \times 10^{12}$ ,  $P = 2.53 \times 10^{-9}$ ,  $n_{MSN} = 22,116,844$  event-neurons,  $n_{CHI} = 153,680$  event-neurons from 10 sessions in 6 animals), compared to an MSN event (blue). **c**, Change in coincident MSN activity (MSN co-activity) following a MSN calcium event (blue), a PV calcium event (orange) or a CHI calcium event (green) from all animals and normalized to event onset for all three types ( $t = 0$ ). Plots are mean  $\pm$  s.e.m. A magnified inset demonstrating the change in MSN co-activity probability in the 100 ms following a MSN, PV or CHI calcium event is shown to the right. Following a CHI calcium event there is an increase in MSN co-activity, whereas following a PV calcium event there is a reduction in MSN co-activity relative to the change in MSN-triggered co-activity (pairwise two-sided z-tests, PV-MSN versus CHI-MSN,  $z = -40.8$ ,  $P = 0$ ; PV-MSN versus MSN-MSN,  $z = -47$ ,  $P = 0$ ; CHI-MSN versus MSN-MSN,  $z = 20.4$ ,  $P = 0$ . Bonferroni-corrected post hoc for multiple comparisons; raw proportions, MSN:  $3.52 \times 10^{-3}$ , PV:  $2.30 \times 10^{-3}$ , CHI:  $5.91 \times 10^{-3}$ ,  $n_{CHI} = 38,189,238$ ,  $n_{CHI} = 38,189,238$  event-pairs,  $n_{MSN} = 9,644,946,557$  event-pairs,  $n_{PV} = 48,285,061$  event-pairs, across all 12 animals and 28 sessions). **d**, Time series showing MSN-MSN event co-activity during laser stimulation of PV cells (orange) and CHIs (green) during laser stimulation in PV-Chrismos mice ( $n = 4$  PV-Chrismos mice and  $n = 4$  Chat-Chrismos mice). For reference, shown in blue is the change in MSN-MSN co-activity around random MSN events from all time periods outside of optogenetic stimulation for all PV-Chrismos and Chat-Chrismos mice. Plots are mean  $\pm$  s.e.m. **e**, Population line plots quantifying the change in MSN-MSN co-activity following optogenetic stimulation of PVs or CHIs in PV-Chrismos and Chat-Chrismos mice. Opto-stimulation-induced co-activity was compared to the endogenous rate of MSN-MSN co-activity from the non-opto-stimulation periods of the imaging session, indicated by the dashed blue line. Error bars and center are mean  $\pm$  s.e.m. During optogenetic stimulation of CHIs, MSN-MSN co-activity increased, whereas during optogenetic stimulation of PVs, MSN-MSN co-activity decreased relative to the endogenous MSN-MSN co-activity rate (pairwise two-sided z-tests,  $n_{CHI} = 2,078,751$  event-pairs,  $n_{MSN} = 694,475,807$  event-pairs,  $n_{PV} = 682,922$  event-pairs; CHI-MSN versus PV-MSN  $z = 78.7$ ,  $P = 0$ ; MSN-MSN versus MSN-PV,  $z = -228$ ,  $P = 0$ ; MSN-MSN versus CHI-MSN,  $z = 19.2$ ,  $P = 0$ ,  $n = 4$  PV-Chrismos mice and  $n = 4$  Chat-Chrismos mice, Bonferroni-corrected post hoc test for multiple comparisons). \* $P < 0.05$ , \*\* $P < 0.01$ , \*\*\* $P < 0.001$ . **f**, Change in movement speed after peaks in MSN-MSN co-activity events (see Supplementary Methods), binned into 500 ms windows for analysis. Error bars and center are mean  $\pm$  s.e.m. Peaks in MSN co-activity were followed by decreases in speed similar to those observed following CHI events and CHI optogenetic stimulation (Friedman test, main effect of time,  $n = 2,249$  peaks in co-activity,  $X^2(8) = 520$ ,  $P < 0.001$ ; Tukey's HSD post hoc (versus 0–0.5 s) 0.5–1.0 s,  $P = 0.030$ , 1.00–1.50 s,  $P = 9.30 \times 10^{-7}$ , 1.50–4.50 s, all  $P = 8.97 \times 10^{-8}$ ; mean ranks, 5.81, 5.54, 5.35, 5.04, 4.84, 4.72, 4.62, 4.52 and 4.56, respectively).

as described previously<sup>12,14</sup>, we found that neither PV nor CHI interneuron populations showed a similar anatomical specificity. Furthermore, we discovered that PV populations became active before MSNs at movement onset and that their calcium activity remained elevated throughout the duration of movement. PVs were also the best predictor of MSN population activity. Interestingly, both endogenous and optogenetically triggered PV activity resulted

in a reduction in the probability of coincident calcium events occurring in the MSN population. PV interneuron-mediated feed-forward inhibition has been hypothesized as a potential mechanism for shutting down active MSNs that are not important for the currently activated motor plan and our data support this model<sup>35</sup>.

Although PV cells can provide powerful and reliable feed-forward inhibition to nearby MSNs<sup>19,38</sup>, our data also suggest that their

activity largely coincides with periods of movement when MSNs are under the influence of strong excitatory cortical input, subcortical input and dopamine release. As such, PV signals indeed may serve as an important component for ‘silencing’ non-motor-relevant MSNs to create a ‘de-noised’ output condition to facilitate movement execution. This process could aid in the selection of individual motor choices through reducing the activity of output neurons that are not integral to ongoing behavior, and our data provide support for this interpretation. Furthermore, given the narrower anatomical space over which PVs were correlated with MSNs, it is possible that specific subpopulations of PVs could be recruited to inhibit nearby MSNs to bias striatal output. Our finding that PV stimulation could spur new movement and modulate the trajectory of ongoing movement suggests that ill-timed PV activation may be a prominent component of hyperkinetic movement disorders, whereas refined coordination of striatal activity by this population is important for specific movements<sup>21,39</sup>. Taken together, our data support the hypothesis that PV cells play a major role in refining the activation of MSNs to modulate movement execution<sup>21,40</sup>. Future studies will be needed to understand the mechanisms by which this process occurs, but recent evidence suggests that PV neurons can influence MSN networks through direct monosynaptic connections and larger-scale di-synaptic circuit interactions<sup>30</sup>.

In contrast to MSNs and PVs, increased activity in CHIs was associated with a reduction in ongoing locomotion. We found that activity between CHIs was largely uncorrelated during voluntary movement, suggesting that the synchronized activity in CHIs observed in previous studies may be related to a specific response to salient environmental stimuli<sup>41–43</sup>. CHI activity did, however, coincide with recruitment and synchronization of MSNs (Fig. 7c), as well as reductions in velocity (Fig. 2h). Using optogenetics, we were able to completely recapitulate (Figs. 3b and 7d,e) each of these findings, illustrating that a major function for CHIs is to coordinate networks of MSNs to trigger the end of a movement bout, and this may represent a key mechanism for cholinergic modulation of motor control. Previous studies in striatal slices have revealed complex actions of acetylcholine in the striatum, including both excitatory and inhibitory effects, that can alter MSN activity states<sup>24,44</sup>. The processes by which acetylcholine may organize MSN networks *in vivo* are less well understood, although the conditions associated with disease states provide some insight. Elevated cholinergic tone has been hypothesized to contribute to Parkinson’s disease symptoms, in particular akinesia and bradykinesia<sup>28,45</sup>, and our results support the idea that augmented cholinergic activity in disease states may promote a pathological synchronization of striatal networks, freezing the dorsal striatum in a state that inhibits movement. The present data offer mechanistic insight into the therapeutic benefits of anti-cholinergic compounds in the treatment of Parkinson’s disease<sup>45,46</sup> and other motor disorders associated with elevated cholinergic tone<sup>28</sup>. As recent studies have implicated phasic dopamine release as a mechanism within the striatum to promote movement<sup>17,48</sup>, our findings suggest that acetylcholine may act in opposition to this process. More specifically, striatal dopaminergic and cholinergic systems may act synergistically to promote or inhibit movements, respectively, and balanced activation within these systems could be critical for the capacity of striatal networks to support dynamic behaviors.

The results reported here specifically relate to striatal control of volitional movement, deficits in which are prominent features of several disorders. Interestingly, evidence suggests that goal-directed actions are often preserved in patients with neurodegenerative disorders such as Parkinson’s disease<sup>2,49,50</sup>. Thus identifying how MSN and interneuron populations interact to control self-generated locomotion is a crucial step in the effort to develop new treatments for a major, debilitating symptom of these disorders. Our data provide a foundation and, more broadly, highlight that as potential therapies

for movement disorders are explored, striatal function should not be considered as a monolithic whole, but rather a mosaic of projection cell networks differentially regulated by neuromodulators and local interneurons to support diverse functions.

## Online content

Any methods, additional references, Nature Research reporting summaries, source data, statements of data availability and associated accession codes are available at <https://doi.org/10.1038/s41593-019-0341-3>.

Received: 22 October 2018; Accepted: 18 January 2019;  
Published online: 25 February 2019

## References

1. Albin, R. L. et al. Increased ventral striatal monoaminergic innervation in Tourette syndrome. *Neurology* **61**, 310–315 (2003).
2. Albin, R. L., Young, A. B. & Penney, J. B. The functional anatomy of basal ganglia disorders. *Trends Neurosci.* **12**, 366–375 (1989).
3. Obeso, J. A. et al. Pathophysiology of the basal ganglia in Parkinson’s disease. *Trends Neurosci.* **23**, Suppl, S8–S19 (2000).
4. Penney, J. B. Jr & Young, A. B. Striatal inhomogeneities and basal ganglia function. *Mov. Disord.* **1**, 3–15 (1986).
5. Mailly, P., Aliane, V., Groenewegen, H. J., Haber, S. N. & Deniau, J. M. The rat prefrontostriatal system analyzed in 3D: evidence for multiple interacting functional units. *J. Neurosci.* **33**, 5718–5727 (2013).
6. Voorn, P., Vanderschuren, L. J., Groenewegen, H. J., Robbins, T. W. & Pennartz, C. M. Putting a spin on the dorsal-ventral divide of the striatum. *Trends Neurosci.* **27**, 468–474 (2004).
7. Graveland, G. A. & DiFiglia, M. The frequency and distribution of medium-sized neurons with indented nuclei in the primate and rodent neostriatum. *Brain Res.* **327**, 307–311 (1985).
8. Tepper, J. M., Wilson, C. J. & Koós, T. Feedforward and feedback inhibition in neostriatal GABAergic spiny neurons. *Brain Res. Rev.* **58**, 272–281 (2008).
9. Gerfen, C. R. et al. D1 and D2 dopamine receptor-regulated gene expression of striatonigral and striatopallidal neurons. *Science* **250**, 1429–1432 (1990).
10. DeLong, M. R. Primate models of movement disorders of basal ganglia origin. *Trends Neurosci.* **13**, 281–285 (1990).
11. Parker, J. G. et al. Diametric neural ensemble dynamics in parkinsonian and dyskinetic states. *Nature* **557**, 177–182 (2018).
12. Barbera, G. et al. Spatially compact neural clusters in the dorsal striatum encode locomotion relevant information. *Neuron* **92**, 202–213 (2016).
13. Cui, G. et al. Concurrent activation of striatal direct and indirect pathways during action initiation. *Nature* **494**, 238–242 (2013).
14. Klaus, A. et al. The spatiotemporal organization of the striatum encodes action space. *Neuron* **96**, 949 (2017).
15. Meng, C. et al. Spectrally resolved fiber photometry for multi-component analysis of brain circuits. *Neuron* **98**, 707–717.e4 (2018).
16. Oorschot, D. E. Cell types in the different nuclei of the basal ganglia. *Handbook Behav. Neurosci.* **20**, 63–74 (2010).
17. Roberts, R. C., Gaither, L. A., Peretti, F. J., Lapidus, B. & Chute, D. J. Synaptic organization of the human striatum: a postmortem ultrastructural study. *J. Comp. Neurol.* **374**, 523–534 (1996).
18. Tepper, J. M. & Bolam, J. P. Functional diversity and specificity of neostriatal interneurons. *Curr. Opin. Neurobiol.* **14**, 685–692 (2004).
19. Tepper, J. M., Tecuapetla, F., Koós, T. & Ibáñez-Sandoval, O. Heterogeneity and diversity of striatal GABAergic interneurons. *Front. Neuroanat.* **4**, 150 (2010).
20. Gittis, A. H. et al. Selective inhibition of striatal fast-spiking interneurons causes dyskinesias. *J. Neurosci.* **31**, 15727–15731 (2011).
21. Gittis, A. H., Nelson, A. B., Thwin, M. T., Palop, J. J. & Kreitzer, A. C. Distinct roles of GABAergic interneurons in the regulation of striatal output pathways. *J. Neurosci.* **30**, 2223–2234 (2010).
22. Koós, T. & Tepper, J. M. Inhibitory control of neostriatal projection neurons by GABAergic interneurons. *Nat. Neurosci.* **2**, 467–472 (1999).
23. Bolam, J. P., Wainer, B. H. & Smith, A. D. Characterization of cholinergic neurons in the rat neostriatum. A combination of choline acetyltransferase immunocytochemistry, Golgi-impregnation and electron microscopy. *Neuroscience* **12**, 711–718 (1984).
24. Calabresi, P., Centonze, D., Gubellini, P., Pisani, A. & Bernardi, G. Acetylcholine-mediated modulation of striatal function. *Trends Neurosci.* **23**, 120–126 (2000).
25. Surmeier, D. J., Ding, J., Day, M., Wang, Z. & Shen, W. D1 and D2 dopamine-receptor modulation of striatal glutamatergic signaling in striatal medium spiny neurons. *Trends Neurosci.* **30**, 228–235 (2007).

26. Yan, Z., Flores-Hernandez, J. & Surmeier, D. J. Coordinated expression of muscarinic receptor messenger RNAs in striatal medium spiny neurons. *Neuroscience* **103**, 1017–1024 (2001).
27. Cachope, R. et al. Selective activation of cholinergic interneurons enhances accumbal phasic dopamine release: setting the tone for reward processing. *Cell Rep.* **2**, 33–41 (2012).
28. Kondabolu, K. et al. Striatal cholinergic interneurons generate beta and gamma oscillations in the corticostriatal circuit and produce motor deficits. *Proc. Natl Acad. Sci. USA* **113**, E3159–E3168 (2016).
29. Chen, T. W. et al. Ultrasensitive fluorescent proteins for imaging neuronal activity. *Nature* **499**, 295–300 (2013).
30. Lee, K. et al. Parvalbumin interneurons modulate striatal output and enhance performance during associative learning. *Neuron* **93**, 1451–1463.e4 (2017).
31. Pinto, L. & Dan, Y. Cell-type-specific activity in prefrontal cortex during goal-directed behavior. *Neuron* **87**, 437–450 (2015).
32. Klapoetke, N. C. et al. Independent optical excitation of distinct neural populations. *Nat. Methods* **11**, 338–346 (2014).
33. Schwartz, T. H. et al. Networks of coactive neurons in developing layer 1. *Neuron* **20**, 541–552 (1998).
34. Wilson, C. J., Chang, H. T. & Kitai, S. T. Firing patterns and synaptic potentials of identified giant aspiny interneurons in the rat neostriatum. *J. Neurosci.* **10**, 508–519 (1990).
35. Moyer, J. T., Halterman, B. L., Finkel, L. H. & Wolf, J. A. Lateral and feedforward inhibition suppress asynchronous activity in a large, biophysically-detailed computational model of the striatal network. *Front. Comput. Neurosci.* **8**, 152 (2014).
36. Smith, K. S. & Graybiel, A. M. Habit formation coincides with shifts in reinforcement representations in the sensorimotor striatum. *J. Neurophysiol.* **115**, 1487–1498 (2016).
37. Thorn, C. A., Atallah, H., Howe, M. & Graybiel, A. M. Differential dynamics of activity changes in dorsolateral and dorsomedial striatal loops during learning. *Neuron* **66**, 781–795 (2010).
38. Owen, S. F., Berke, J. D. & Kreitzer, A. C. Fast-spiking interneurons supply feedforward control of bursting, calcium, and plasticity for efficient learning. *Cell* **172**, 683–695.e15 (2018).
39. Kalanithi, P. S. et al. Altered parvalbumin-positive neuron distribution in basal ganglia of individuals with Tourette syndrome. *Proc. Natl Acad. Sci. USA* **102**, 13307–13312 (2005).
40. Planert, H., Szydłowski, S. N., Hjorth, J. J., Grillner, S. & Silberberg, G. Dynamics of synaptic transmission between fast-spiking interneurons and striatal projection neurons of the direct and indirect pathways. *J. Neurosci.* **30**, 3499–3507 (2010).
41. Adler, A., Katabi, S., Finkes, I., Prut, Y. & Bergman, H. Different correlation patterns of cholinergic and GABAergic interneurons with striatal projection neurons. *Front. Syst. Neurosci.* **7**, 47 (2013).
42. Apicella, P. Tonically active neurons in the primate striatum and their role in the processing of information about motivationally relevant events. *Eur. J. Neurosci.* **16**, 2017–2026 (2002).
43. Kimura, M., Rajkowski, J. & Evarts, E. Tonically discharging putamen neurons exhibit set-dependent responses. *Proc. Natl Acad. Sci. USA* **81**, 4998–5001 (1984).
44. Shen, W., Hamilton, S. E., Nathanson, N. M. & Surmeier, D. J. Cholinergic suppression of KCNQ channel currents enhances excitability of striatal medium spiny neurons. *J. Neurosci.* **25**, 7449–7458 (2005).
45. Lang, A. E. & Lees, A. J. Anticholinergic therapies in the treatment of Parkinson's disease. *Mov. Disord.* **17 Suppl 4**, S7–S12 (2002).
46. Pisani, A. et al. Targeting striatal cholinergic interneurons in Parkinson's disease: focus on metabotropic glutamate receptors. *Neuropharmacology* **45**, 45–56 (2003).
47. da Silva, J. A., Tecuapetla, F., Paixão, V. & Costa, R. M. Dopamine neuron activity before action initiation gates and invigorates future movements. *Nature* **554**, 244–248 (2018).
48. Howe, M. W. & Dombeck, D. A. Rapid signalling in distinct dopaminergic axons during locomotion and reward. *Nature* **535**, 505–510 (2016).
49. Bichsel, O. et al. Functionally separated networks for self-paced and externally-cued motor execution in Parkinson's disease: evidence from deep brain recordings in humans. *Neuroimage* **177**, 20–29 (2018).
50. Redgrave, P. et al. Goal-directed and habitual control in the basal ganglia: implications for Parkinson's disease. *Nat. Rev. Neurosci.* **11**, 760–772 (2010).

## Acknowledgements

We thank members of the Han Lab for suggestions on the manuscript. We would also like to thank J. Li and E. Kolaczyk for their useful insights on data analysis and statistical analysis. We would also like to acknowledge C. Harvey and D. Dombeck for their help on the construction of the 3D spherical tracking system. This work was supported by the NIH Director's Office (No. 1DP2NS082126 to X.H.), NINDS (Nos. 1R01NS081716 and 1R01NS087950 to X.H.), the Grainger Foundation (to X.H.) and the Pew Foundation (to X.H.).

## Author contributions

W.M.H. and H.J.G. performed all experiments. M.R. and D.Z. analyzed the data. M.B. contributed software for video processing and data analysis. X.H. supervised the study. W.M.H, H.J.G, M.R., A.G.D and X.H. wrote the manuscript and contributed to the interpretation of the results. A.G.D. and M.K. provided consultation on both statistical analysis and permutation tests. V.S. provided consultation on both calcium imaging data analysis and generalized linear models.

## Competing interests

The authors declare no competing interests.

## Additional information

**Supplementary information** is available for this paper at <https://doi.org/10.1038/s41593-019-0341-3>.

**Reprints and permissions information** is available at [www.nature.com/reprints](http://www.nature.com/reprints).

**Correspondence and requests for materials** should be addressed to X.H.

**Journal peer review information** *Nature Neuroscience* thanks Tianyi Mao and other anonymous reviewer(s) for their contribution to the peer review of this work.

**Publisher's note:** Springer Nature remains neutral with regard to jurisdictional claims in published maps and institutional affiliations.

© The Author(s), under exclusive licence to Springer Nature America, Inc. 2019

## Methods

**Animal surgery.** All animal procedures were approved by the Boston University Institutional Animal Care and Use Committee. Combined experiments included data from mice expressing Cre recombinase in either choline acetyltransferase-expressing cells (Chat-Cre;  $n=14$ ; GM24Gsat) or parvalbumin (Pvalb)-expressing cells (PV-Cre mice;  $n=14$ ; B6;129P2-Pvalb<sup>mlcre/Arb/J</sup>), 8–12 weeks old at the start of the experiments. Both male and female mice were used in this study and breeders were obtained commercially (Chat-Cre, Mutant Mouse Resource Center; and PV-Cre, Jackson Laboratory). One cohort of mice was used for imaging studies without optogenetic laser illumination ( $n=6$  Chat-Cre mice, and  $n=6$  PV-Cre mice). Mice first underwent surgery for implantation of a sterilized custom imaging window with an attached guide cannula that was assembled before surgery. The window/guide assembly consisted of a stainless steel imaging cannula (outer diameter 0.317 cm, inner diameter 0.236 cm, height 2 mm), fitted with a circular coverslip (size 0, outer diameter 3 mm) adhered using an ultraviolet-curable optical adhesive (Norland Products). The guide cannula (26 gauge; No. C135GS4; Plastics One) was fixed at a 45° angle and terminated flush to the base of the imaging window. To access the dorsal striatum, the overlying cortical tissue was carefully aspirated away to expose the corpus callosum as an anatomical guide. The white matter was carefully thinned until the underlying striatal tissue could be visualized via a surgical microscope. The imaging window was then lowered in place and centered over the dorsal striatum (anteroposterior +0.5 mm, mediolateral 1.8 mm, dorsoventral –1.6 mm from brain surface). During the same surgery, a custom aluminum head-plate was attached to the skull, anterior to the imaging cannula. Following complete recovery (14–21 days after surgery), animals were injected with a 1  $\mu$ l cocktail containing 500 nl AAV9-Syn-GCaMP6f.WPRE.SV40 (titer  $6.6 \times 10^{12}$  GC ml<sup>-1</sup>) and 500 nl AAV9-CAG-flex-tdTomato.WPRE.SV40 virus (titer  $5.1 \times 10^{12}$  GC ml<sup>-1</sup>) through the attached guide cannula. Virus was delivered via a 10  $\mu$ l syringe (No. 701N, Hamilton Company) controlled by a micro-infusion pump (UltraMicroPump3-4, World Precision Instruments) fitted with a 33 gauge infusion cannula (No. C135IS4, Plastics One).

A second cohort of mice was used for the behavioral and network analysis during optogenetic experiments ( $n=16$  combined;  $n=4$  for each group analysis; PV-Cre mice expressing Chrimson-tdTomato, Control PV-Cre mice expressing tdTomato without Chrimson, Chat-Cre mice expressing Chrimson-tdTomato and Control Chat-Cre mice expressing tdTomato without Chrimson). These animals were prepared in a similar way to the description above, except that virus infusion for tdTomato or Chrimson-tdTomato was performed in a separate procedure 10 days before window implantation. Mice were infused with either AAV9-CAG-flex-tdTomato (opto-controls) or AAV9-Syn-flex-Chrimson-tdTomato (opto-group). To ensure the maximal expression of Chrimson or tdTomato within the imaging hemisphere, a total volume of 3  $\mu$ l was delivered at two depths (1.5  $\mu$ l: anteroposterior +0.5 mm, mediolateral 1.8 mm, dorsoventral –3.5 mm; and 1.5  $\mu$ l: anteroposterior +0.5 mm, mediolateral 1.8 mm, dorsoventral –2.3 mm). Injections were delivered via pressure ejection (10–15 per square inch, 15–20 ms pulses delivered at 0.5 Hz) through a glass pipette (diameter 1.2 mm) pulled to a sharp point and then broken at the tip to a final inner diameter of ~20  $\mu$ m. The pipette was lowered over 3 min and allowed to remain in place for a further 3 min before infusion began. The injection occurred at a rate of 100 nl min<sup>-1</sup>, and 10 min elapsed before raising the pipette to the second location. At the conclusion of the second infusion, an additional 10 min delay was introduced before the pipette was slowly withdrawn over 2–3 min. AAV9-Syn-flex-Chrimson was obtained from the University of North Carolina Vector Core: WPRE.SV40 virus (titer  $5.9 \times 10^{11}$  GC ml<sup>-1</sup>). Following window implantation surgery and after complete recovery (14–21 days after surgery), 500 nl AAV9-Syn-GCaMP6f.WPRE.SV40 (titer  $6.6 \times 10^{12}$  GC ml<sup>-1</sup>) was infused through the attached guide cannula as described earlier.

**Animal habituation.** Following surgery and virus infusion (typically about 21–28 days), mice were first handled for several days before being head-fixed to the treadmill/imaging apparatus. Mice were then habituated to running on the spherical treadmill while head-fixed for two weeks, 3–4 days per week, at the same time of day as subsequent recording sessions. Each animal received at least six habituation sessions before the first recording day. The cohort of mice used in the optogenetic studies underwent the same handling and habituation protocol, but with four or five additional sessions. Habituation was performed in the dark at the same light illumination intensity that would be used for recording sessions. Habituation sessions were the same duration as imaging sessions.

**Data acquisition.** *Image acquisition with a scientific complementary metal oxide semiconductor camera.* Animals were positioned underneath the microscope and imaged while freely running on the spherical treadmill. Image acquisition was performed with a custom microscope equipped with a scientific complementary metal oxide semiconductor camera (ORCA-Flash4.0 LT Digital CMOS camera, No. C11440-42U, Hamamatsu). GCaMP6f fluorescence excitation was accomplished with a 5 W light-emitting diode (No. LZ1-00B200, 460 nm; LedEngin). tdTomato fluorescence excitation was accomplished with a 1,000 mA light-emitting diode (No. LXML-PX02-0000, 567 nm, Lumileds). The custom microscope included a Leica N Plan 10×0.25 PH1 microscope objective lens, a dual-band excitation

filter (No. FF01-468/553-25), a dichroic mirror (No. FF493/574-Di01-25×36), a dual-band emission filter (No. FF01-512/630-25; Semrock) and a commercial single light reflex lens focused to infinity as the tube lens (Nikon Zoom-NIKKOR 80–200 mm f/4 AI-s). The camera when coupled to a 10× objective lens yielding an imaging field of view of  $1.343 \times 1.343$  mm<sup>2</sup>, with each pixel corresponding to  $1.312 \times 1.312$   $\mu$ m<sup>2</sup>.

A custom MATLAB script was used to trigger frame capture and to synchronize image acquisition with movement. Digital transistor-transistor logic (TTL) trigger pulses were delivered to the camera using a common input/output interface (No. USO-6259, National Instruments). Image acquisition was performed using HC Image Live (HC Image Live; Hamamatsu). The time interval between image frame captures was  $47.0 \pm 0.2$  ms (~21.3 Hz, mean ± standard deviation,  $n=28$  sessions). For each image frame, exposure time was fixed at 20 ms. Image data were stored in multi-page tagged image file format. For a recording session of 10 min, approximately 24 gigabytes of image data were stored, spread across six video files. The acquisition software was configured to buffer all frames in computer random access memory to optimize speed. At the conclusion of the GCaMP6f imaging session, we imaged tdTomato fluorescence for ~10 s (50 frames at 20 ms or 200 ms exposure per frame) to identify GCaMP-expressing interneurons.

**Optogenetic laser equipment and protocol.** A 635 nm 200 mW red diode laser (Shanghai Laser Optics and Century Co.) was coupled to the imaging scope via an optical fiber (No. BFL48-200, Thor Labs) with the fiber tip focused to illuminate the entire imaging window from above. Laser illumination was under digital transistor-transistor logic control using the image acquisition software HC Image Live (HC Image Live, Hamamatsu). Briefly, a 15 ms pulse was initiated 10 ms after camera readout concluded, and another image frame capture could not begin until a minimum of 5 ms had passed since the laser illumination digital transistor-transistor logic pulse ended. The average sampling rate across optogenetic sessions was slower ( $63.4 \pm 0.4$  ms per sample (±s.e.m.) for the Chrimson and control sessions) due to the requirements of a 15 ms laser pulse in the imaging loop.

Before each imaging session, laser output was adjusted to 10 mW at the height of the imaging cannula window using a light meter calibrated for 635 nm wavelength (No. PM100D, Thor Labs). Optogenetic recording sessions were identical to other imaging sessions described earlier, but with 13–23 laser stimulation trials. Laser trials occurred randomly within a session, but each trial was separated by  $40 \pm 15$  s. A laser trial consisted of 100 light pulses, 15 ms per pulse, delivered between imaging exposures (at ~15 Hz). All four groups of animals underwent two recording sessions with 3–7 days between sessions.

**Movement data acquisition.** The spherical treadmill was constructed following the design of Dombeck et al.<sup>51</sup>. Briefly, the treadmill consisted of a three-dimensional (3D) printed plastic housing and a Styrofoam ball supported by air. Movement was monitored using two computer universal serial bus mouse sensors affixed to the plastic housing at the equator of the Styrofoam ball. Each sensor was mounted 3–4 mm away from the surface of the ball, and 78 degrees apart. The  $x$ - and  $y$ -surface displacement measured by each sensor was acquired using a separate computer running a Linux OS (minimal CentOS 6). A simple, multi-threaded python script was used to send packaged  $\langle dx, dy \rangle$  data at 100 Hz to the image acquisition computer via a RS232 serial link. Packaged motion data were received on the imaging computer using a MATLAB script, and synchronized to each acquired frame. Because of a delay in initiating movement sensor data capture, we excluded the first 5 s of the motion data (following interpolation) and imaging data (following event identification) from the beginning of every recording session in the subsequent analysis.

**ROI calcium trace processing and calcium event characterization. Image preprocessing: contrast enhancement, motion correction and baseline subtraction.** Image frames underwent several preprocessing steps before trace extraction<sup>52</sup>. Briefly, we first applied homomorphic filtering to each image frame to enhance contrast, and then performed motion correction using cross-correlation between a given image frame and a reference frame. The reference frame was updated by sequential addition of each corrected frame. Baseline subtraction was performed using a two-step process. We first identified the minimum fluorescence for each pixel across the first 2,047 frames of each recording session (~96 s), and spatially convolved the minimum fluorescence throughout the whole image field to determine the background value for each pixel. We then subtracted this value from each frame. In the second step, we subtracted the average intensity of pixels with the lowest dynamic range within the first 2,047 frames of the recording sessions from all pixels within a frame, and set the lower pixel value boundary to 0. Each frame was then converted to a uint8 file format.

**ROI identification and ROI ΔF/F trace extraction.** Several semi-automatic algorithms have been developed for ROI identification<sup>52–54</sup>. However, we found that these algorithms were not sufficiently robust in identifying all neurons in the striatum. Thus, we manually selected ROIs based on morphology using a circle with a radius of 6 pixels (7.8  $\mu$ m), from single-frame representations of the recording session. To identify PV or CHI cells, we first processed the tdTomato

video as described in image pre-processing above but without background subtraction. We further smoothed each image with a spatial filter (a square spatial Gaussian filter of width 5 pixels and a standard deviation of 0.8). Images were then thresholded to reveal the brightest 5% pixels corresponding to PV and CHI cells.

Region of interest fluorescence was calculated as the average intensity across all pixels in the circle. In instances when a small number of pixels overlapped between two ROIs, the overlapping pixels were assigned to only one of the labeled ROIs. We interpolated fluorescence time series, so that consecutive data were 0.0469 s apart, using the MATLAB function `interp1 ('t', pchip)`.  $\Delta F/F$  was calculated as the fluorescence at each time point minus the mean, and then divided by the mean.

**Calcium event identification.** Two types of calcium event were detected. The first we considered ‘transient’, with a fast rise and decay, and the other we considered ‘slow’, with a delayed rise and long decay. Each cell was first assigned to one of these two categories through manual inspection. We found that 1.9% of neurons had both transient and slow calcium event characteristics. These neurons were excluded from further analyses. To identify individual calcium events,  $\Delta F/F$  calcium traces were first smoothed using a moving average of 21 points, scaled by a value of 1.05. We then de-trended the  $\Delta F/F$  calcium traces by subtracting a local minimum value for each time point, defined as the minimum value within a radius of 500 data points of the smoothed trace, similar to ref.<sup>55</sup>. For transient calcium events, we identified all points with fluorescence exceeding three standard deviations above the mean computed from the non-event portion of the trace. We iteratively performed this step, where the points above threshold were excluded from future iterations. Consecutive points above this threshold were then grouped as a putative event, plus one data point before the onset. If the addition of the single data point resulted in two overlapping putative events, these were grouped into one event. Calcium events overlapping with the start or the end of a recording session were discarded. Finally, only events with maximum amplitude exceeding five standard deviations of the baseline were considered a calcium event.

For slow calcium events, we further smoothed ‘de-trended  $\Delta F/F$ ’ with the MATLAB function ‘`sgolayfilt`’, with an order of three polynomial and 101 data points. We then identified all points using the same methods as described for transient calcium events, except using a threshold of two standard deviations above the mean.

Laser-induced calcium events, manually identified as those coincident with laser onset, have durations between the transient and slow calcium events. For these events, we first high-pass-filtered the  $\Delta F/F$  calcium traces at  $\sim 2 \times 10^{-5}$  Hz (MATLAB commands ‘`butter`’ with arguments 2 and 0.0005, and then ‘`filtfilt`’ for zero-phase filtering). We then identified all points using the same methods as described for transient calcium events, using a threshold of two standard deviations above the mean.

After removal of the first 5 s of the fluorescence traces due to motion artifact as described previously, events continuous with the beginning of the shortened session were not considered for further analysis.

**Calcium event property calculation.** To characterize calcium events from each cell type we first subtracted the baseline, calculated as the mean of the 20 data points before each event onset from the event time series. To estimate AUC for transient calcium events, we further smoothed these events with a 21-point moving average filter before baseline subtraction. Rise time was calculated as the time from calcium event onset, the first data point of a calcium event, to the peak. To compute AUC, peak width and calcium event amplitude, we added one extra data point to each event after event termination. To compare calcium event properties between high- and low-speed time periods, calcium events were first averaged for each ROI and then compared across all neurons. ROIs that did not have an event in either low- or high-speed time period were excluded from the respective statistical testing.

**Deconvolution of calcium traces.** Deconvolution occurred by labeling the rising phase of a calcium event, including the event maximum, as ones (active regions) and the rest as zeroes. Deconvolved calcium traces are used in Figs. 2h, 4d,e, 5a–c and 7c–f.

**Movement data analysis. Linear velocity calculation.** We first calibrated the spherical treadmill by pinning the two sides of the ball at the equator for physical distance, or at the top and the bottom for rotation. Linear velocity in perpendicular X and Y directions is calculated as:

$$X = \frac{L - R \cos \theta}{\cos(\frac{\pi}{2} - \theta)}$$

$$Y = R$$

where  $L$  is the vertical reading from the left sensor,  $R$  is the vertical reading from the right sensor and  $\theta$  is the angle between the sensors (78 degrees).  $X$  or  $Y$  values corresponding to velocities exceeding  $100 \text{ cm s}^{-1}$  were excluded. Then,  $X$  and  $Y$

values were interpolated at 21.3 Hz as fluorescence signals and linear velocity  $D$  was computed as

$$D = (X^2 + Y^2)^{\frac{1}{2}}$$

**Rotational velocity calculation and directional preference.** To compute rotational velocity, lateral readings from both computer sensors were first converted to radians  $\text{s}^{-1}$  and then averaged. Readings corresponding to angular velocities exceeding a magnitude of  $15 \text{ radians s}^{-1}$  were excluded. Readings were then converted to angular displacement, interpolated at 21.3 Hz and then converted to rotational velocity.

**Identification of sustained periods of movement with high and low linear velocity.** We identified periods of high versus low linear velocity similarly to Barbera et al.<sup>12</sup>. Briefly, we first smoothed linear velocity traces using a 1.5 Hz low-pass filter (MATLAB commands ‘`butter`’ and then ‘`filtfilt`’ for zero-phase filtering). Periods of high-speed movement were identified as the time periods with linear velocity exceeding  $5 \text{ cm s}^{-1}$  for more than 2 s (43 data points). Similarly, periods of low-speed movement were those where linear velocity remained below  $1 \text{ cm s}^{-1}$  for more than 2 s. Periods overlapping with the beginning or end of the session were excluded.

**Movement onset, offset and peak velocity identification.** To identify movement onset, offset and peak velocity, we used the unsmoothed linear velocity trace. To identify movement onsets, we first identified acceleration transition points as those when linear velocity rose to above  $5 \text{ cm s}^{-1}$ . A movement onset was then defined as the second data point before the transition points where velocity remained  $\leq 5 \text{ cm s}^{-1}$  for at least  $\sim 500 \text{ ms}$  (10 data points) before, and exceeded  $40 \text{ cm s}^{-1}$  at some point within  $\sim 1,000 \text{ ms}$  (20 data points) after. To identify movement offsets, we first identified deceleration transition points as those when linear velocity decreased to below  $5 \text{ cm s}^{-1}$ . Movement offset was defined as the point before the deceleration transition point where velocity exceeded  $15 \text{ cm s}^{-1}$  within  $\sim 500 \text{ ms}$  before, and also remained  $\leq 5 \text{ cm s}^{-1}$  for at least  $\sim 500 \text{ ms}$  after the transition point. Peak velocity was identified as local maximum using the MATLAB function `findpeaks`, which was then thresholded at  $55 \text{ cm s}^{-1}$ . To identify rotational onsets, we identified the acceleration transition point when absolute rotational velocity increased to above  $0.5 \text{ radians s}^{-1}$ . A rotation onset was then identified as the second data point before the transition point where velocity remained  $\leq 0.5 \text{ radians s}^{-1}$  for at least  $\sim 500 \text{ ms}$  before, and also exceeded  $2 \text{ radians s}^{-1}$  within  $\sim 1,000 \text{ ms}$  after. Movement onsets and offsets that extended beyond the length of the session were truncated to the beginning and end of the session.

**Relationship between calcium activity and movement. Movement-triggered calcium fluorescence.** Population movement-triggered fluorescence was computed on  $\Delta F/F$  values from each neuron over 100 time points (Supplementary Figs. 4, and 7), or 200 time points (Fig. 2d,f), on either side of each movement event (onset, offset and peak velocity). All recording sessions from all mice were used. Error bar plots were plotted neuron-wise, and the value for each neuron is the mean of the 40 data points before or after each movement event. These neuron-wise averages and statistics were computed after first identifying and averaging windows of 50 time points on either side of each event for each neuron.

To compare the timing of maxima in fluorescence around velocity peaks, we examined a window of 100 time points before and after each velocity peak. We constructed a mixed-effects model, averaging fluorescence values over a 6 s window for each neuron, grouped in 1 s bins, beginning 2 s before each velocity peak. Models were fitted using the maximum-likelihood MATLAB function `fitlme`, and  $P$  values were determined using the residual degrees of freedom. The full mixed-effects model appeared as, in Wilkinson notation:

$$\text{Fluorescence} \sim 1 + \text{Time} \times \text{Cell\_type} + (1|\text{Event\_ID}) + (1|\text{Cell\_ID}) + (1|\text{Mouse})$$

where Time refers to the time bin and Cell\_type to the genotype of the respective cell. Random intercepts were included for each mouse (Mouse), for each individual cell (Cell\_ID) and for each peak-velocity event (Event\_ID). In these models, we identified the time period of maximum fluorescence by finding the bin with the highest expected value. After identifying a significant interaction term between Time and Cell\_type, we broke up this model by cell type.  $P$  values were corrected using the Benjamini–Hochberg procedure after pooling all  $P$  values across all time bin comparisons to baseline in all models (15 total comparisons)<sup>56</sup>.

To determine whether a neuron was significantly positively, or negatively, modulated by speed or rotation, we used one-tailed rank-sum tests to compare the fluorescence values of the 40 data points before versus after an identified movement onset, using a  $P$  value threshold of 0.025. Neurons were then assigned to one of the four categories: speed-only, rotation-only, conjunctive or neither.

To assess the proportion of neurons positively modulated in the 500 ms before movement onset (Supplementary Fig. 2h), we analyzed the average fluorescence of each neuron during baseline time points ( $-950$  to  $-500 \text{ ms}$  before movement onset) compared to the pre-movement period ( $-450 \text{ ms}$  to movement onset)

using one-sided rank-sum tests with a cutoff of  $P=0.025$ . To quantify the time difference between PV and MSN fluorescence increase at movement onset, we identified the first time point in the movement onset window when the averaged  $\Delta F/F$  trace of all PV cells or MSNs of that session exceeded 0.02. This represents a moderate increase in  $\Delta F/F$  from baseline. The latency between PV cell and MSN responses were then calculated across all sessions where this criterion was met ( $n=13$  sessions in total).

For proximity tests (Supplementary Fig. 9b,c), we first computed the proportion of neurons within 100  $\mu\text{m}$  of a neuron belonging to a certain category. We then compared the proportions surrounding neurons of a given category to those surrounding all other neurons. These two sets of proportions were compared neuron-wise. Neurons without any neighbors were excluded from analysis, and only MSNs were used for this analysis.

**Neuron pairwise asymmetric correlation analysis.** An asymmetric correlation coefficient from neuron A to B was calculated as described previously using deconvolved calcium traces<sup>12,35</sup> and the equation

$$r_{A \rightarrow B} = \frac{n_{A \cap B}}{n_A}$$

That is, the number of events in the deconvolved traces in neuron A that overlapped with events in neuron B was divided by the total number of events in neuron A. Pairwise correlation between neurons A and B was then calculated as the averaged correlation coefficients in both directions, A to B and B to A.

To compute baseline correlation coefficients, the deconvolved traces were randomly shifted circularly and uniformly over the entire length as discussed by Barber et al.<sup>12</sup>. This process was repeated 5,000 times for each neuron pair, and the correlation coefficients of these shifted traces were used to determine significance using one-sided  $P < 0.05$  (Fig. 4). Correlations with deconvolved traces with no events were labeled as NaN, and these were considered not significant. The random values in the plots (Fig. 4d,e) are the mean shuffled correlation coefficients for each neuron pair.

To compare the proportions of neuron pairs with significant correlations that were spatially close ( $<100 \mu\text{m}$ ) or spatially far ( $>750$  and  $<1,500 \mu\text{m}$ ), we constructed a generalized linear model:

$$\text{Is\_significant} \sim 1 + \text{Cell\_pair\_type} \times \text{Distance}$$

where Is\_significant is a random variable corresponding to whether the particular pair is significantly correlated, Cell\_pair\_type is a categorical variable corresponding to MSN–CHI, MSN–MSN or MSN–PV, and Distance is an indicator variable that equals 1 if the pair is spatially far. We used a binomial distribution with an identity link function. To compare differences between the time periods, we compared the interaction terms for all three pair-types.

For Fig. 4a, we used the complete-linkage clustering function of MATLAB (linkage (\*, 'complete'), followed by cluster (\*, 'cutoff', [distance cutoff], 'criterion', 'distance'), where [distance cutoff] was equivalent to 100  $\mu\text{m}$ ). We statistically compared within-cluster and out-of-cluster groups by treating each directional measure of asymmetric correlation as independent, and computed the rank-sum between the directional within-cluster and out-of-cluster groups. In this case, a correlation coefficient from A to B, where B has no events, has a correlation coefficient of 0, and in the opposite case (from B to A), of NaN.

For Fig. 5a, the number of neuron pairs with significant correlations divided by the average number of neuron pairs with significant correlations in all bins were plotted over their anatomical distance. The distance between pairs of neurons centroid(A)–centroid(B) or centroid(B)–centroid(A) was assigned randomly.

**Neuron-pairwise Pearson's correlation analysis.** Because of the sparseness of calcium events during periods of low-speed movement, we used Pearson's correlation (Fig. 4b,c). During each motor bout, the correlation coefficients were determined between each MSN pair and then averaged across all motor bouts for each session. Shuffled traces (1,000 times) were created by concatenating  $\Delta F/F$  values from high- or low-velocity time periods, for each ROI, and circularly shifting each concatenated trace by a random, uniformly distributed value over the length of the trace. Then, the shuffled traces were broken into segments equal to the length of the original high- or low-speed segments. Correlation values for each pair during high- and low-time periods were averaged over all 1,000 repetitions.

**Correlation of MSN subsets with distinct CHI populations.** To examine whether the same set of MSNs was correlated with CHIs that were positively or negatively modulated by movement (Supplementary Fig. 7g), we analyzed sessions with at least one positively movement-modulated CHI and one negatively movement-modulated CHI ( $n=8$  sessions). To test whether MSNs correlated with positively and negatively modulated CHIs belong to different communities, we calculated the Jaccard index of the two sets of MSNs as follows:

$$\text{Jaccard index} = \frac{\text{MSN}_+ \cap \text{MSN}_-}{\text{MSN}_+ \cup \text{MSN}_-}$$

In this equation,  $\text{MSN}_+$  represents the set of MSNs correlated with at least one positively modulated CHI using the pairwise asymmetric correlation analysis, and  $\text{MSN}_-$  represents the set of MSNs correlated with at least one negatively modulated CHI. To test whether the MSNs correlated with these two types of CHI were non-overlapping, we performed a permutation test (Supplementary Fig. 7g). Briefly, we first identified MSNs that exhibited significant correlation with any CHI. We then performed a bootstrapping procedure 5,000 times without replacement. For each CHI, we randomly assigned from this pool of MSNs a number of MSNs equal to the number correlated with the given CHI. Then, a Jaccard index was computed for each iteration.

**Neuron-triggered fluorescence analysis.** Neuron-triggered fluorescence was determined using deconvolved calcium traces (Fig. 7a,b).

In these analyses, triggering events are the time point immediate before calcium event onset. Unless otherwise noted, triggering events within 50 time points of the beginning or 51 time points of the end of the trace were not included for analysis. We centered fluorescence values for each MSN around each triggering event, and compared changes in  $\Delta F/F$  values during the ten data points (~500 ms) after each event using a rank-sum test (ROI event-wise). Standard error of the mean across the entire ~5 s interval was calculated with Welford's algorithm<sup>57</sup>.

**Neuron-triggered speed and rotation.** To analyze changes in velocity following an event in a given cell type, we constructed a mixed-effects model using the MATLAB function 'fitlme' on the normalized data (data were normalized for each cell type to the data point coincident with event onset, by subtracting and then dividing). In Wilkinson notation the model was:

$$\text{Velocity} \sim 1 + \text{Time} \times \text{Cell\_type} + (1 | \text{Mouse}) + (1 | \text{Cell\_ID})$$

Time is a categorical variable corresponding to time bin. Cell\_type corresponds to PV, MSN or CHI in Fig. 2h, or positively or negatively modulated cells in Supplementary Figs. 4h, 7h. We accounted for variance in intercept introduced by each mouse (Mouse) and each individual cell (Cell\_ID). We broke up the model by cell type to test the effect of time by removing all terms relating to cell type, and created smaller models.  $P$  values were corrected for the collections of values obtained from each of the smaller models using the Benjamini–Hochberg procedure.

Neuron-triggered rotation (Supplementary Fig. 8c) was analyzed in a similar way, using the absolute value of the rotational velocity in place of speed.

To determine the rate at which speed changed following a calcium event (Supplementary Fig. 2i), we first computed the normalized event-triggered speed for each neuron. We then used the normalized speed values for each neuron between 0 and 1.5 s after each calcium event to construct a series of simple linear models. These models had predictors including only an intercept and the instantaneous time values, from which we obtained a slope value for each neuron. We compared slope values among the three neuron types using the following linear mixed-effects model:

$$\text{Coefficients} \sim 1 + \text{Cell\_type} + (1 | \text{Mouse})$$

Here, Coefficients represent the slopes of the simple linear models, while Mouse and Cell\_type are as described previously.

**Neuron co-activation analysis.** Co-activation was calculated using deconvolved calcium traces. We calculated the total number of co-active MSN pairs around each triggering event, defined as the data point before calcium event onset, and the total number of possible MSN pairs across all triggering events, for all neurons across all recording sessions. We then calculated the proportion of co-active pairs over all events out of total pairs over all events.

For comparison across neuron types (Fig. 7c), we averaged the two data points following each triggering event subtracted by the value at the triggering point, and the errors of the two data points were propagated. We then used  $z$ -tests for comparison among cell types. Shaded error bar plots (Fig. 7c) are standard error estimates computed from  $\sqrt{\frac{P(P-1)}{n}}$ , where  $P$  is the probability of the neuron pair being co-active at that time point and  $n$  is the number of total pairs over all events. Error bar plots were centered at triggering onset.

To detect changes in movement speed around MSN–MSN peak co-activation (Fig. 7f), we summed the deconvolved traces for all MSNs recorded in each session and identified MSN–MSN co-activation as the point when the summed activity exceeded two standard deviations above the mean. Peak co-activation within each co-activation period is identified as the local maximum. If two local maxima of the same amplitude occurred in the same co-activation period, the first peak was used. Co-activations within 100 time points of the beginning or end of a recording session were excluded.

**Calculation of predictor performance using regression analysis.** To estimate how each cell type predicted movement or population MSN activity (Fig. 6), we built linear models and assessed the model performance using correlations similar to the time series forecasting cross-validation method described by Hyndman and

Athanasiopoulos<sup>58</sup>, and that used by Parker et al.<sup>11</sup>. We used the framework of partitioning a time series into equally sized, temporally continuous sets for training and testing models. Data of the entire session were separated into ten consecutive and equally sized segments. Linear model parameters were determined using nine segments, and the values for the last segment were then predicted using these parameters. The Pearson correlation coefficient between the predicted and actual value of this last segment was used to assess predictive ability. This process was repeated ten times, and the Pearson correlation coefficients were averaged for a given predictor. To plot predicted values for both summed MSN fluorescence and speed, predictors were determined using the entire session.

To predict linear velocity using MSN, PV and CHI cells (Fig. 6d,h), we first binned  $\Delta F/F$  traces and linear speed to 0.1 s bins.  $\Delta F/F$  traces were then combined, and their average z-scored  $\Delta F/F$  value was used as the predictor variable. Next, this predictor along with an intercept was tested using our modified cross-validation. To estimate the predictor performance of MSN subpopulations, a random subsample of MSNs with an equal number of simultaneously recorded interneurons in the session was used. This process was repeated 5,000 times, and the average value was used as the predictor performance for each recording session. For single interneurons and single MSNs, the average value across all single neurons was used as the predictor performance for each session. For sessions in which there was only one interneuron, the mean value over all single MSNs was used as the value of the MSN subpopulation.

To predict MSN population fluorescence (Fig. 6b,f), we used summed population MSN fluorescence as the response variable. Each predictor was binned as above. To estimate the predictor performance of MSN subpopulations, a random subsample of MSNs with equal number of simultaneously recorded interneurons in the session was used, and the MSN population response was calculated without the subsampled MSNs. This process was repeated 5,000 times and the average value was used as the predictor performance. An intercept term was also included in each model. These analyses were also performed using only positively or negatively modulated interneurons (Supplementary Figs. 4i, 7i) for sessions that had at least one positively and one negatively modulated interneuron.

To compare predictor performance (Supplementary Fig. 12), we incorporated cell type into a simple, multivariate mixed-effects model:

$$\text{Velocity} \sim 1 + \text{Fluorescence} + \text{Cell\_type} :$$

$$\text{Fluorescence} + \text{Velocity\_lag1}$$

$$+ \text{Velocity\_lag2} + (1 | \text{Session}) + (1 | \text{Fluorescence} | \text{Cell\_ID})$$

**Cell\_type** is the genotype of the predicting neuron, **Fluorescence** is the z-scored average fluorescence over 0.1 s bins, **Session** is a session ID corresponding to the fluorescence trace and **Cell\_ID** corresponds to each cell. **Velocity** is the z-scored binned velocity, and **Velocity\_lag1** and **Velocity\_lag2** are analogous terms accounting for the autocorrelation of **Velocity** values. For the complete analysis, data from all 28 sessions were used and MSNs were used as the reference cell type variable. To plot this analysis, the above mixed-effects model was also run separately for each session with at least one interneuron (10 CHI sessions and 17 PV sessions), and the coefficient of the interaction term corresponding to **Cell\_type:Fluorescence** was plotted. Because each session was modeled separately, the **(1|Session)** term was excluded from these models. Each dot in this plot corresponds to a coefficient from each of these smaller models, and the lines correspond to the coefficient values from the larger model.

#### Optogenetic activation induced changes in calcium activity and movement.

**Laser-triggered changes in calcium fluorescence, calcium event probability and neuron co-activation.** Region of interest identification, trace extraction and movement data processing were largely the same as described above for non-optogenetic sessions. One session displayed two brief (~2 and ~14 s) large motion artifacts during part of the recording, and we replaced the affected data points with interpolated values. Another session displayed a baseline shift toward the beginning (~50 s), so these data were excluded from further analysis.

To examine laser-induced fluorescence change in MSNs, PV cells and CHIs (Supplementary Fig. 11), we aligned the  $\Delta F/F$  of each cell to laser illumination period. The difference in fluorescence following laser stimulation onset (20 time points) versus the 20 time points immediately before laser onset was compared cell-wise.

To examine the change in calcium event probability, we used deconvolved calcium traces (Supplementary Fig. 11e,f). Event probability was aligned to laser onset for each neuron, and we normalized the event probability by averaging across all sessions the respective neuron type in the corresponding mice.

To examine changes in neuron co-activation (Fig. 7d,e), we first computed MSN–MSN co-activation at the onset of MSN triggering events during the non-laser time period by averaging the two time points immediately following each event onset. Events within 50 time points of the beginning or end of the session were not included. To compute the mean co-activation of MSN–MSN pairs during each laser period, all neuron pairs were combined after normalizing co-activation values by dividing by the mean co-activation during non-laser epochs. This was also repeated for non-laser epochs (Fig. 7e). To plot MSN-triggered co-activation

during non-laser periods (Fig. 7d), we analyzed the 50 time points on either side of the triggering event after discarding events within 100 time points of the beginning or end of a recording session. To plot the laser-triggered MSN–MSN co-activation time series, we plotted the mean and standard error of the mean across all time points after normalizing via the previously mentioned Welford's algorithm<sup>57</sup>.

For MSN- and laser-triggered co-activation for both Chat-Chrison and PV-Chrison mice, we used pairwise z-tests and the sample means and sample standard errors of the means as estimates to test significance. Figure 7e was plotted event-pairwise with event-pairs included from all sessions.

**Laser-triggered changes in movement velocity.** We calculated normalized movement velocity to movement speed immediately before each laser onset, and then subtracted 1 to represent changes. To test whether there was a significant change in speed during laser activation, we used a linear mixed-effects model on the normalized velocity. Our models appear as follows:

$$\begin{aligned} \text{Velocity} \sim & 1 + \text{Time} + (1 | \text{Mouse}) + (1 | \text{Event\_ID}) + (1 | \text{TimeBin} | \text{Event\_ID}) \\ & + (1 | \text{Mouse} | \text{Event\_ID}) \end{aligned}$$

**Event\_ID** here corresponds to unique laser epochs. We tested for a significant main effect of time using ANOVA on this model, and computed post hoc t-tests for each time bin versus the time bin at time  $t=0$ .  $P$  values were corrected within each model using the Benjamini–Hochberg procedure. We separated data into those events occurring only in sustained low-speed time periods, and then repeated the analysis on these smaller datasets. Fig. 3b,c is plotted event-wise.

**Laser-triggered changes in direction.** To distinguish between vigorous directional change from small rotational velocity changes associated with balancing behavior, we set a threshold where directional changes exceeding 1 radian  $s^{-1}$  were counted as vigorous directional changes. To quantify whether there were more vigorous directional changes during laser-on versus laser-off time periods, we identified all directional changes for each session and compared the probability of such changes during each laser-on versus laser-off time period across all sessions. We compared the difference in the probabilities of directional changes during the rising and falling phases of PV or CHI calcium events (including events continuous with the beginning of the session), versus other time periods (Supplementary Fig. 8a,c), neuron-wise.

**Correlations of MSN activity with laser-induced PV activation.** To examine the uniformity of PV influence on MSNs while the population of PV interneurons was activated optogenetically, we calculated the number of MSNs that had significant asymmetric correlation coefficients during optogenetic stimulation in PV-Chrison-tdT mice. This analysis was identical to the neuron-pairwise asymmetric correlations described above in non-optogenetic mice. To compute significance, we randomly and circularly shifted the deconvolved MSN traces 5,000 times to generate a distribution of randomly shifted MSN traces. We then computed the asymmetric correlation coefficients between the randomly shifted MSN traces and laser-on time periods. To test whether PV optogenetic activation homogeneously affected the MSN population (Supplementary Fig. 4g), we randomly sampled with replacement 10,000 times the binary values to determine whether or not an MSN was significantly correlated with laser-on time periods. We compared the proportion of MSNs significantly correlated to zero by taking the total number of random samples with no significantly correlated values and dividing this by the total number of samples (10,000). We compared the proportions of MSNs to a value of 1 analogously.

**Histology and quantification.** At the end of the experiments, all mice were transcardially perfused and tissue was processed to confirm both GCaMP6f and tdTomato expression, and cannula placement. Mice were perfused with 30 ml 0.01M phosphate buffered saline (Fisher Scientific, No. BP2944-100), followed by 30 ml 4% paraformaldehyde (Sigma Aldrich, No. 158127). Brains were carefully removed and post-fixed overnight in 4% paraformaldehyde before being transferred to 30% sucrose solution. Brains were sectioned horizontally at a thickness of 40  $\mu m$  with a freezing microtome (CM 2000R, Leica). Tissue sections were collected throughout the striatum. A subset of sections (4–6 sections per animal) were stained with antibodies against PV (rabbit anti-PV, SWANT PV25, 1:1,000) or Chat (goat anti-Chat antibody, Millipore, No. AB144P 1:500), followed by Alexa Fluor 633 goat anti-rabbit secondary antibody for PV staining (Invitrogen, No. A11011, 1:1,000) or Alexa Fluor 633 donkey anti-goat secondary antibody for Chat staining (Life Technologies, No. A21082, 1:200). Antibodies and dilution concentrations were previously reported<sup>59,60</sup>. Briefly, sections were rinsed with 0.05 M Tris-HCl buffer (Tris, pH 7.6), followed by a 60 min rinse in blocking buffer containing 5% serum and 0.2% Triton. Sections were incubated for 24 h with primary antibody. Sections were then rinsed three times (10 min each) in Tris-HCl and incubated with the secondary antibody for 2 h. Sections were rinsed again and mounted on gelatin-coated slides using anti-fade mounting medium (Vectashield, No. H-1400).

Confocal images were taken on an Olympus FV1,000 scanning confocal microscope using a 60 $\times$  water immersion lens. All images were comprised of

Z-stacks taken at 5  $\mu\text{m}$  intervals throughout the 40  $\mu\text{m}$  slices. Stacks were taken from horizontal sections as near as possible to the bottom of the imaging window, and all imaging stacks were taken within 1 mm of the imaging plane. Areas were chosen to include similarly dense tdTomato cell counts across animals by an experimenter blinded to the animal strain. To confirm targeting specificity, each tdTomato<sup>+</sup> cell was categorized as immuno-positive or -negative for the antibody stain. We also quantified the number of immuno-positive cells from each stack that were tdTomato<sup>+</sup> to estimate the infection efficiency near the imaging window. We analyzed between two and four non-overlapping confocal stacks from four to six slices per animal from a large subset of animals that comprised our GCaMP imaging dataset ( $n = 7$  PV-Cre and  $n = 7$  Chat-Cre mice). Cell counts were pooled across slices stained for the same marker for each animal, and averaged to produce a single data point for quantification.

**Statistical tests.** Sample sizes were estimated based on neuron yields from pilot studies and published anatomical descriptions of PV and CHI population densities, using G\*Power 3.1.9.2. We applied a two-tailed Wilcoxon–Mann–Whitney test utilizing a  $\beta/\alpha$  ratio of 1.0 and an effect size of 0.5. Additional assumptions included the expectation of 300 neurons per recording and PV and CHI density of 2.5% in all cells. Our sample sizes are also consistent with previous publications of calcium imaging in the striatum.<sup>14,38,51</sup>

Researchers were aware of the animal strain at the time of recording, but analysis was done offline by a researcher who was unaware of cell identity. For histology experiments, areas were chosen to include similarly dense tdTomato cell counts across animals by an experimenter blinded to the animal strain.

Data recording sessions were randomized between PV and Chat animals over the course of the study. Optogenetic stimulations sessions were randomized in Chrimson and tdT control animals, with several non-stimulation days occurring between the two sessions. For all calcium imaging sessions, no direct replication was performed although each animal was subjected to calcium imaging up to three times and data were collapsed together for analysis. For confocal images, we analyzed between two and four non-overlapping confocal stacks from four to six slices, which were pooled together per animal and averaged for quantification.

The detailed statistical tests are described above in the analysis. Briefly, the following statistical tests were used in this study: Chi-square, Wilcoxon rank-sum, sign-tests, Kruskal–Wallis, Friedman, Fisher, binomial, z-tests and Pearson's correlation. When conducting non-parametric tests we did not make any assumptions of data, including normality. For z-tests, the sample sizes of the distributions were sufficiently large that, according to the central limit theorem, their means were expected to follow normal distributions. If present in a sign-test, ties were removed from consideration automatically and their presence was noted in the manuscript. All values that evaluated to NaN were treated as missing data.

All tests were two-tailed unless noted otherwise; post hoc tests were conducted using the MATLAB function multcompare following a Kruskal–Wallis or a Friedman test. Use of this function was noted in the manuscript as Tukey's HSD, as it utilizes for both Kruskal–Wallis and Friedman Tukey-like procedures for non-parametric data.

Data were plotted using neuron-weighted averages unless otherwise noted. Standard error of the mean was computed using the standard formula, based on

the assumption of normality of the mean regardless of the shape of the underlying distribution whose mean we describe. Because non-parametric statistics are used throughout the manuscript, estimated standard errors of the mean are shown primarily as a tool for visualization. Unless otherwise noted, box plots were constructed via the MATLAB function boxplot, and outliers were removed for visualization. Outliers were determined automatically by the boxplot function. These were defined as data points that were greater than the third quartile value plus 1.5-fold the distance between quartile three and quartile one, or data points that were less than the first quartile value minus 1.5-fold the distance between quartile three and quartile one.

**Reporting Summary.** Further information on research design is available in the Nature Research Reporting Summary linked to this article.

## Code availability

All source code and custom scripts for analysis will be made available on request.

## Data availability

The raw data that support the findings of this study are available from the corresponding author upon request.

## References

51. Dombeck, D. A., Khabbaz, A. N., Collman, F., Adelman, T. L. & Tank, D. W. Imaging large-scale neural activity with cellular resolution in awake, mobile mice. *Neuron* **56**, 43–57 (2007).
52. Mohammed, A. I. et al. An integrative approach for analyzing hundreds of neurons in task performing mice using wide-field calcium imaging. *Sci. Rep.* **6**, 20986 (2016).
53. Mukamel, E. A., Nimmerjahn, A. & Schnitzer, M. J. Automated analysis of cellular signals from large-scale calcium imaging data. *Neuron* **63**, 747–760 (2009).
54. Pnevmatikakis, E. A. et al. Simultaneous denoising, deconvolution, and demixing of calcium imaging data. *Neuron* **89**, 285–299 (2016).
55. Jia, H., Rochefort, N. L., Chen, X. & Konnerth, A. In vivo two-photon imaging of sensory-evoked dendritic calcium signals in cortical neurons. *Nat. Protoc.* **6**, 28–35 (2011).
56. Reiner, A., Yekutieli, D. & Benjamini, Y. Identifying differentially expressed genes using false discovery rate controlling procedures. *Bioinformatics* **19**, 368–375 (2003).
57. Knuth, D. E. *The Art of Computer Programming* (Addison-Wesley, Boston, 2005).
58. Hyndman, R. J. & Athanasopoulos, G. *Forecasting: Principles and Practice* (OTexts, Melbourne, 2013).
59. James, N. M., Gritton, H. J., Kopell, N., Sen, K. & Han, X. Muscarinic receptors regulate auditory and prefrontal cortical communication during auditory processing. *Neuropharmacology* **144**, 155–171 (2019).
60. Keaveney, M. K. et al. A microRNA-based gene-targeting tool for virally labeling interneurons in the rodent cortex. *Cell Rep.* **24**, 294–303 (2018).

## Reporting Summary

Nature Research wishes to improve the reproducibility of the work that we publish. This form provides structure for consistency and transparency in reporting. For further information on Nature Research policies, see [Authors & Referees](#) and the [Editorial Policy Checklist](#).

### Statistics

For all statistical analyses, confirm that the following items are present in the figure legend, table legend, main text, or Methods section.

n/a Confirmed

- The exact sample size ( $n$ ) for each experimental group/condition, given as a discrete number and unit of measurement
- A statement on whether measurements were taken from distinct samples or whether the same sample was measured repeatedly
- The statistical test(s) used AND whether they are one- or two-sided  
*Only common tests should be described solely by name; describe more complex techniques in the Methods section.*
- A description of all covariates tested
- A description of any assumptions or corrections, such as tests of normality and adjustment for multiple comparisons
- A full description of the statistical parameters including central tendency (e.g. means) or other basic estimates (e.g. regression coefficient) AND variation (e.g. standard deviation) or associated estimates of uncertainty (e.g. confidence intervals)
- For null hypothesis testing, the test statistic (e.g.  $F$ ,  $t$ ,  $r$ ) with confidence intervals, effect sizes, degrees of freedom and  $P$  value noted  
*Give P values as exact values whenever suitable.*
- For Bayesian analysis, information on the choice of priors and Markov chain Monte Carlo settings
- For hierarchical and complex designs, identification of the appropriate level for tests and full reporting of outcomes
- Estimates of effect sizes (e.g. Cohen's  $d$ , Pearson's  $r$ ), indicating how they were calculated

*Our web collection on [statistics for biologists](#) contains articles on many of the points above.*

### Software and code

Policy information about [availability of computer code](#)

Data collection

All collection was performed using Matlab 2016a and the commercial software Hamamatsu HC Image. All source code and custom scripts used for collection will be made available at time of publication and are available to reviewers and editors during review.

Data analysis

All analysis was performed using Matlab 2016b. All source code and custom scripts for analysis will be made available at time of publication and are available to reviewers and editors during review.

For manuscripts utilizing custom algorithms or software that are central to the research but not yet described in published literature, software must be made available to editors/reviewers. We strongly encourage code deposition in a community repository (e.g. GitHub). See the Nature Research [guidelines for submitting code & software](#) for further information.

### Data

Policy information about [availability of data](#)

All manuscripts must include a [data availability statement](#). This statement should provide the following information, where applicable:

- Accession codes, unique identifiers, or web links for publicly available datasets
- A list of figures that have associated raw data
- A description of any restrictions on data availability

All raw data and custom functions to produce each figure will be made available at time of publication and are available to reviewers and editors during review.

# Field-specific reporting

Please select the one below that is the best fit for your research. If you are not sure, read the appropriate sections before making your selection.

- Life sciences     Behavioural & social sciences     Ecological, evolutionary & environmental sciences

For a reference copy of the document with all sections, see [nature.com/documents/nr-reporting-summary-flat.pdf](http://nature.com/documents/nr-reporting-summary-flat.pdf)

## Life sciences study design

All studies must disclose on these points even when the disclosure is negative.

Sample size	Sample sizes were estimated based on neuron yields from pilot studies and published anatomical descriptions of PV and ChAT population densities. A compromised power analysis was performed using G*Power 3.1.9.2 ( <a href="http://www.gpower.hhu.de">http://www.gpower.hhu.de</a> ). We applied a two tailed Wilcoxon-Mann-Whitney test utilizing an $\beta/\alpha$ ratio=1.0, an effect size of 0.5. Additional assumptions included the expectations of 300neurons/recording and PV and ChAT density of 2.5% of all cells. Applying these assumptions resulted in $\alpha$ and $\beta$ probabilities of <0.1 with 6+ subjects of each genotype background.
Data exclusions	No animals were excluded from this manuscript. A subset of traces (1.9%) were not analyzed because they contained both slow and fast calcium dynamics making automated selection of calcium events impractical. We found no evidence that these traces were more pronounced in any of the cell classes we identified (PV, MSN, or ChAT). Please see Supplemental Methods Page 6, paragraph 5, for details.
Replication	No direct replication was performed although each animal was subject to calcium imaging 1-3 times and data was collapsed together for analysis.
Randomization	There were no treatment conditions to compare in this study. All recording sessions days were randomly performed with PV-cre and ChAT-cre genotyped animals intermixed across days.
Blinding	Partially: On recording days, animals backgrounds were known. Trace extraction and calcium signals were analyzed with the investigators unaware of which neurons belonged to each cell class or the genotype of the animal being analyzed.  For histology - sections were selected and images were taken from slides by a researcher not aware of genotype or antibody used. Cells were also counted and quantified from these sections by a researcher blinded to the genotype of the animal or antibody used.

## Reporting for specific materials, systems and methods

We require information from authors about some types of materials, experimental systems and methods used in many studies. Here, indicate whether each material, system or method listed is relevant to your study. If you are not sure if a list item applies to your research, read the appropriate section before selecting a response.

Materials & experimental systems		Methods	
n/a	Involved in the study	n/a	Involved in the study
<input type="checkbox"/>	<input checked="" type="checkbox"/> Antibodies	<input checked="" type="checkbox"/>	<input type="checkbox"/> ChIP-seq
<input checked="" type="checkbox"/>	<input type="checkbox"/> Eukaryotic cell lines	<input checked="" type="checkbox"/>	<input type="checkbox"/> Flow cytometry
<input checked="" type="checkbox"/>	<input type="checkbox"/> Palaeontology	<input checked="" type="checkbox"/>	<input type="checkbox"/> MRI-based neuroimaging
<input type="checkbox"/>	<input checked="" type="checkbox"/> Animals and other organisms		
<input checked="" type="checkbox"/>	<input type="checkbox"/> Human research participants		
<input checked="" type="checkbox"/>	<input type="checkbox"/> Clinical data		

## Antibodies

Antibodies used	Primary Antibodies against PV (rabbit anti-PV, SWANT PV25 1:1000, Primary anti-ChAT antibody, Millipore AB144P 1:500, Alexa Fluor 633 donkey anti-goat secondary antibody for ChAT staining (Life Technologies, A21082 1:200), Alexa Fluor 633 goat anti-rabbit secondary antibody for PV staining (Invitrogen A21070, 1:1000)
Validation	PV: <a href="https://www.swant.com/pdfs/PV27_Rabbit_anti_Parvalbumin.pdf">https://www.swant.com/pdfs/PV27_Rabbit_anti_Parvalbumin.pdf</a> : Absence of AB staining in PV knock out mice. Validated in mice and rat. Also see 1. Kretsinger R.H. (1981) Neurosci. Res. Progr. Bull. 19/8, MIT-Press 2. Celio M.R., Heizmann C.W. (1981) Nature 293: 300-302

3. Celio M.R., Heizmann C.W. (1982) Nature 297:504-506
4. Schwaller B., et al. (1999) Am. J. Physiol. 276. C395-403
5. \*Filice F, Celio M.R., Szabolcsi V. (2017) JCN, in press

ChAT: see website for validation studies: [http://www.emdmillipore.com/US/en/product/Anti-Choline-Acetyltransferase-Antibody\\_MM\\_NF-AB144P](http://www.emdmillipore.com/US/en/product/Anti-Choline-Acetyltransferase-Antibody_MM_NF-AB144P): Validated in mice and rats.

Secondaries: Validation:

<https://www.thermofisher.com/antibody/product/Donkey-anti-Goat-IgG-H-L-Cross-Adsorbed-Secondary-Antibody-Polyclonal/A-21082>

<https://www.thermofisher.com/antibody/product/Goat-anti-Rabbit-IgG-H-L-Cross-Adsorbed-Secondary-Antibody-Polyclonal/A-21070>

## Animals and other organisms

Policy information about [studies involving animals](#); [ARRIVE guidelines](#) recommended for reporting animal research

Laboratory animals	Combined experiments included data from both ChAT-Cre mice (n=14; GM24Gsat) and PV-cre mice (n=14; B6;129P2-Pvalbtm1(cre)Arbr/J), 8–12 week old at the start of the experiments, both male and female, were used in this study (Chat-Cre: Mutant Mouse Resource Center, Davis, CA; and PV-cre: Jackson Laboratory, Maine)
Wild animals	N/A
Field-collected samples	N/A
Ethics oversight	All animal procedures were approved by the Boston University Institutional Animal Care and Use Committee

Note that full information on the approval of the study protocol must also be provided in the manuscript.